POLITECNICO DI TORINO

Master's Degree in Electronic Engineering (Devices and Technologies for Integrated Electronics and Optoelectronics)

Master's Degree Thesis

Ordered mesoporous carbon decorated with metal oxides: a comparison of amorphous and crystalline WO_3 for energy storage applications

Supervisors

Prof. Andrea LAMBERTI

Mara SERRAPEDE

Juqin ZENG

Candidate

Pedram HOSSEINI

July 2021

Summary

The sustained growth rate of renewable energy sources and widespread utilization of portable electronic devices have underlined the demands for efficient portable energy storage with high rate capability and large specific capacity. Subsequently, electrochemical energy storage (EES) is considered a cut-edging technology in energy applications, as it accounts for providing high specific power and capacity in addition to low cost and long cycling stability.

Tungsten oxide and mesoporous carbon structure have both caused attraction due to their long life cycle and less environmental impact, in addition to the high theoretical capacity of the former and high specific surface area of the latter material. In this project, a hybrid material produced from ordered mesoporous carbon and WO_3 ($OMC - WO_3$) is investigated as the active material of half electrochemical cells. The storage properties highly depend on the nature of the carbonaceous material (providing a high surface area with low electrical resistance) and the investigated metal oxide structures (WO_3) (e.g., phases and degree of crystallinity). Both $OMC - WO_3$ and OMC are tested in water-based (0.5 M H_2SO_4) cells and aprotic-based coin cells (1 M $LiPF_6$ in EC:DMC).

OMC is obtained by the hard-template method through the carbonization of sucrose into the mesopores of the SBA-15 silica. The hybrid powder is synthesized by impregnating phosphotungstic acid with OMC, followed by thermal decomposition in the N2 atmosphere in three different temperatures, including 300, 400, 600 °C, which leads to three different samples. Regarding the XRD and FE-SEM observations, the first two hybrid materials are amorphous while WO_3 crystals appear after the thermal annealing at 600 °C. Evidently, the $OMC - WO_3 - 400$ aqueous cell and $OMC - WO_3 - 600$ aprotic coin cell stored the highest specific energies with 732 mAh/g (scan rate = 5 mV/s after 5000 cycles) and 114 mAh/g (current density = 560 mA/g after 1600 cycles), respectively. Therefore, as the future reference in the design of high-performance EES devices, the hybrid material can be considered as an anode, and pristine OMC can be a possible choice for the cathode.

Acknowledgements

I would like to thank the most important person in my life, my wife Shiva ANSARIPOUR, for her patience and motivation during my education. Without her, I would not have the ability to achieve my goals in academic life.

I express my gratitude to my thesis supervisor Dr. LAMBERTI for his supports and guidance, besides providing all facilities to accomplish my research in the following project.

I also thank Mrs. SERRAPEDE for her advice and guidance during this project. Her knowledge definitely helped me to improve my scientific and practical experiences in electrochemical concepts.

Finally, I must thank my parents for their supports and efforts in facilitating my progress.

Table of Contents

List of Tables

List of Figures

Acronyms

EES
Electrochemical Energy Storage

OMC
Ordered Mesoporous Carbon

EDL
Electrical Double Layer

EDLC
Electrical Double Layer Capacitor

SC
Super Capacitor

EC
Electrochemical Capacitors

LIB
Lithium-ion Battery

CV
Cyclic Voltammetry

GCD
Galvanostatic Charge/Discharge

WE
Working Electrode

RE

Reference Electrode

CE

Counter Electrode

AC

Active Carbon

CPE

Constant Phase Element

EIS

Electrochemical Impedance Spectroscopy

ESR

Equivalent Series Resistance

PW

Potential Window

SHE

Standard Hydrogen Electrode

SEI

Solid Electrolyte Interface

XRD

X-ray Diffraction

SEM

Scanning Electron Microscope

FESEM

Field Emission Electron Microscopic

EDX

Energy Dispersive X-ray spectroscopy

GITT

Galvanostatic Intermittent TitrationTechnique

CB

Carbon Black

PVDF

Polyvinylidene Fluoride

OCP

Open Circuit Potential

Chapter 1

Introduction

1.1 Energy Storage Devices

The sustained growth rate of renewable energy sources, such as solar and wind systems, has increased the demands of energy storage devices with high performance and efficiency properties. In addition, the widespread utilization of portable electronics devices, wireless network systems, and anticipated Internet of Things, which expect portable energy storage with high rate capability and large capacity, has turned the study of electrochemical energy storage (EES) into an imperious concern. Consequently, achieving an EES device with high specific power and capacity in addition to low cost and long cycling stability is essential [1, 2].
The fundamental elements of EES devices are positive and negative electrodes and the electrolyte, acting as a medium between two electrodes for the transportation of positive and negative ions [3]. The energy-storage process at the electrodes and electrolyte interface depends on whether the EES device has a capacitive or battery-like behavior (will be discussed more in 1.2). Figure 1.1 shows three different possible electrochemical energy storage properties, including batteries, pseudocapacitors, and supercapacitors, which might work based on either faradaic or non-faradaic (electrical double layer (EDL)) mechanisms [2].

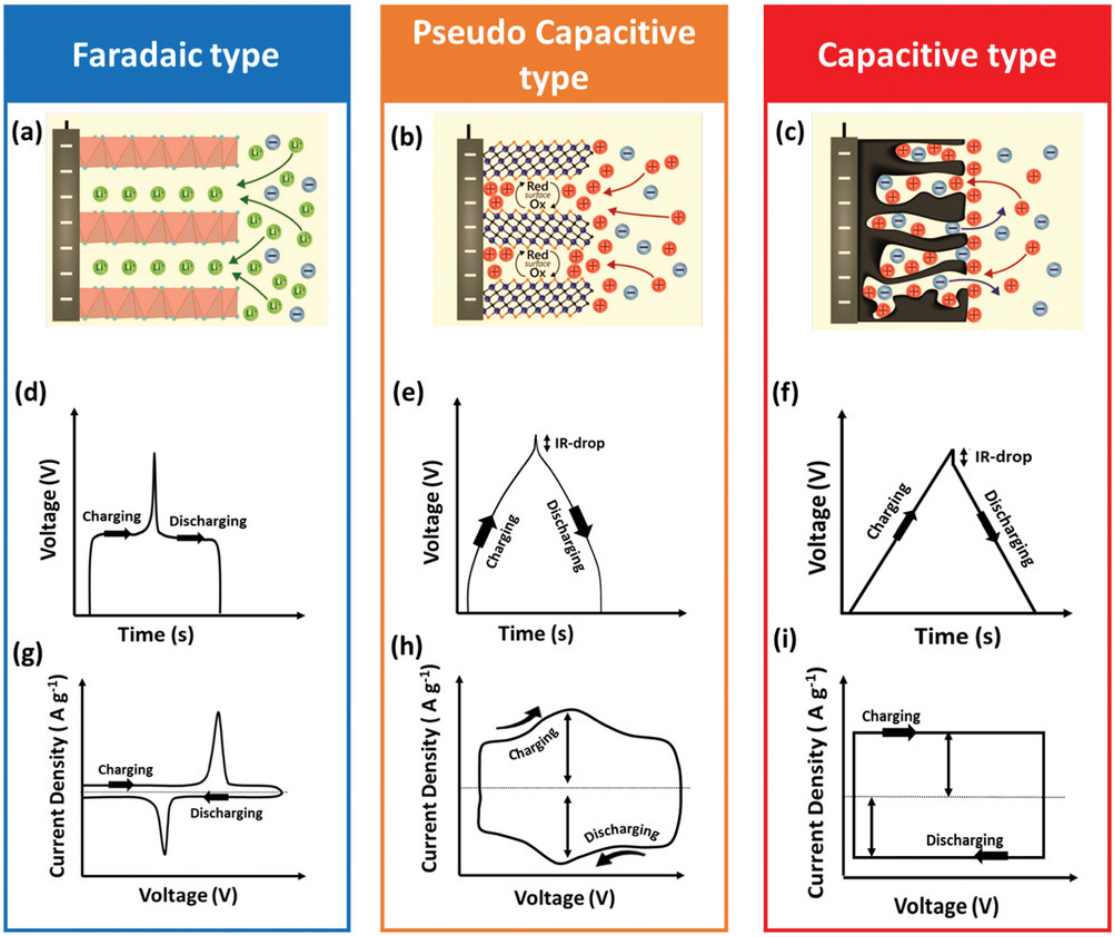

Figure 1.1: Three types of charge storage mechanisms and EES devices: (a) faradaic, (b) pseudocapacitive, (c) electric double layer capacitive. Typical galvanostat and voltammetric behaviour of (d)(g) batteries, (e)(h) pseudocapacitors, and (f)(i) electric double layer capacitors [2]

In the following section, short introductions and comparison of the most commercially available EES devices, including lithium-ion batteries (LIB) and supercapacitors (SC), are presented.

1.1.1 Batteries

Thanks to the high specific capacity that batteries can usually provide, they are known as the most commercially available EES devices [4]. Their charge storage mechanism is mainly based on a redox reaction at the interface between the electrolyte and a bulk electrode. If the redox reaction is reversible, the EES is known as a rechargeable battery. These reversible reactions can be classified into alloy

reaction, conversion reaction, and insertion/extraction categories (Figure 1.2) [5]. The significant volume enlargement in alloy reaction and also the large voltage hysteresis in conversion reaction result in the electrodes cracking and poor efficiency in these EES devices. Extraction/insertion (intercalation) reaction is the most common in the high power rechargeable batteries and pseudocapacitors, as the volume variation of electrodes is small and the reversibility of the reaction is high. In addition to the type of chemical reaction, high electronic and ionic conductivities of the electrodes and electrolyte, respectively, are necessary for high power EES device [2].

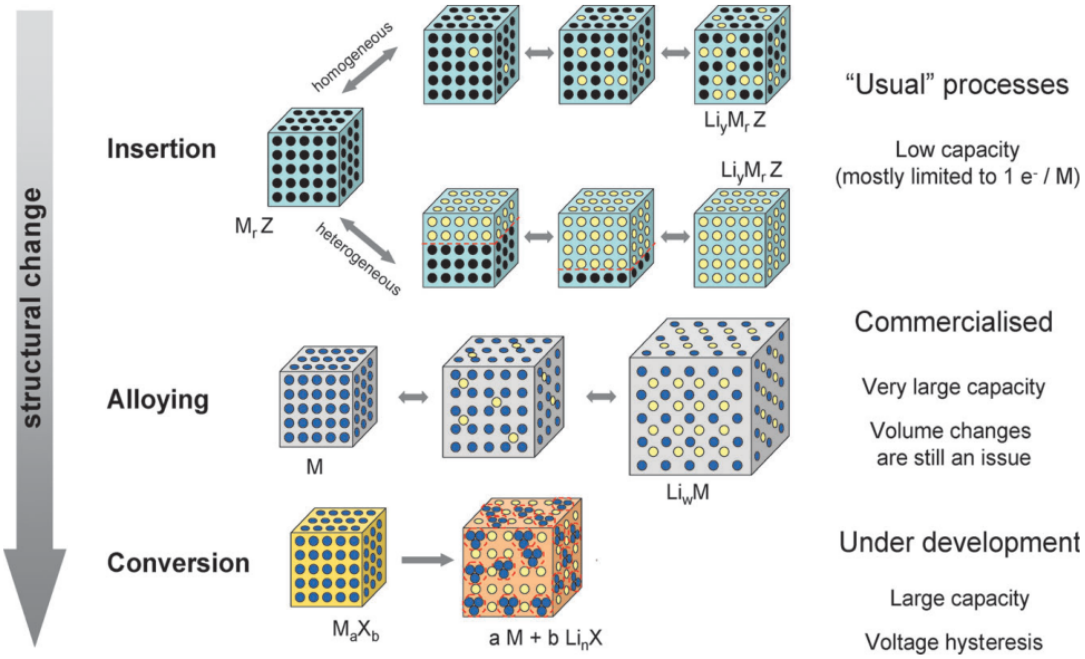

Figure 1.2: Different charging/discharging reactions obtained in Li-ion batteries. In the crystal structure the black spheres are voids, yellow spheres are Li, and blue spheres are are metal. [5]

Li-ion batteries (LIB) are the most popular rechargeable energy storage, especially in portable devices, such as electronic devices and electrical vehicles (EVs). The charging storage process is based on the Li-ions intercalation reaction on electrodes. The positive and negative electrodes are separated by an electrolyte solution containing Li^+ cation in Li-ion electrochemical cell. However, due to lithium's resource limitations, new types of batteries, such as sodium-ion (SIBs) and potassium-ion batteries, which have a considerable amount of resources on the earth, have been introduced as state-of-the-art technologies [6].

1.1.2 Conventional capacitors and supercapacitors

The conventional capacitors, known as their remarkably high power charge/discharge process, are made by two parallel conductive plates and a thin layer of electrically insulating (dielectric) layer sandwiched between them. The energy storage principle of these devices is based on the electrostatic field across the plates. One type of EES is electrochemical capacitors (EC) or supercapacitors (SC). They store a higher amount of charges than conventional capacitors thanks to the high surface area of the positive or negative electrodes of SCs. Besides, they propose higher rate capability but lower energy density in comparison with rechargeable batteries. The so-called non-faradaic charge storage mechanism takes action at the electrolyte and electrode (usually made by carbon-based nanostructures) interface through the adsorption of electrolyte ions into the electrode nanostructure (e.g., pores). Consequently, since no chemical reaction happens, unlike rechargeable batteries, the charge-storage process is faster, the life cycle of such EES devices is higher and the charging process is more secure than batteries [4, 7, 8]. Moreover, the high-tensile strain capability of SCs has made them suitable to be flexible in order to use the in wearable applications [6, 9].

1.1.3 Energy and Power density analysis (Ragone Plot)

As mentioned before, the electrical energy storage devices have different charging/discharging power and energy density, depending on their energy-storage mechanism. As a result, the Ragone plot is introduced to compare different energy storage devices in terms of power and energy density. The Ragone plot, presented with an x-y log scale axis, gives two primary information about energy storage devices:

- The power limitation of energy storage devices.
- The optimum region where the device gives optimum values of energy and power.

The rate capability and capacity of EES devices are limited far from the literature values due to the nonideal factors, such as internal resistivity and self-discharging of the device [10].
Figure 1.3, obtained from [7], presents an overall view of the Ragone plot of electrical energy storage devices. The capacitors have a large power, while their poor energy storage ability makes them unsuitable for energy applications. Additionally, a comparison of power and energy density of batteries and SCs, as two primary categories of EES devices, are presented in this figure.

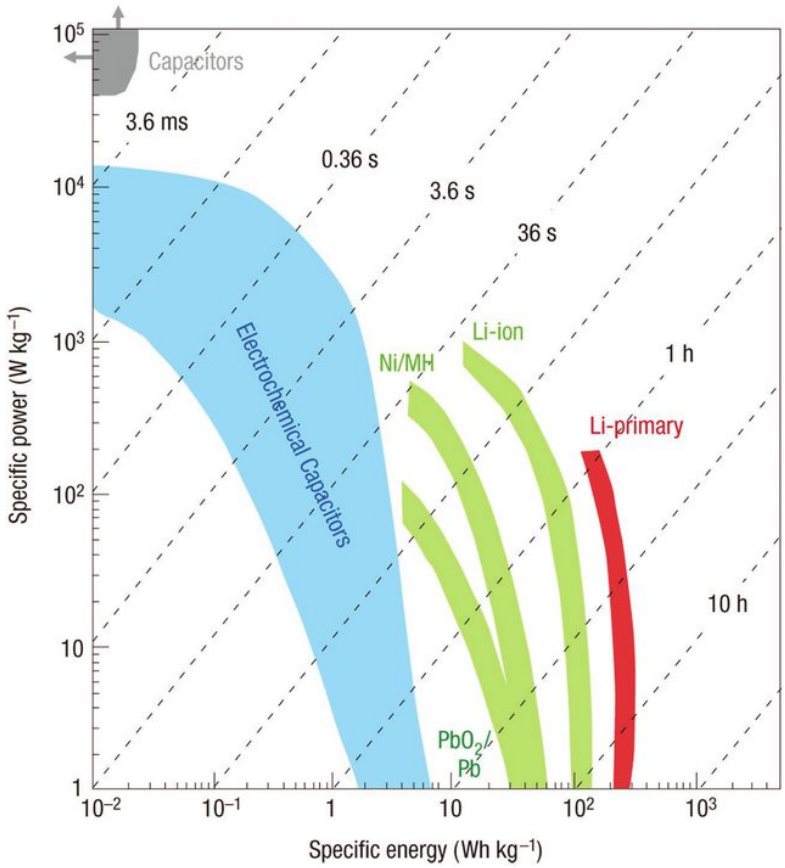

Figure 1.3: Ragone plot to compare different EES devices, in terms of power density and energy density

1.2 Charge storage mechanisms

Electrochemical energy storage can be classified into three categories, depending on the charging storage mechanism [2, 11]:

- **Non-faradiac (electric double layer)**: Charge storage at the interface of electrode and electrolyte which is based on electrostatic interaction.
- **Pseudocapacitors**: Faradaic energy storage mechanism at the surface, based on fast reversible redox reactions at the surface of active material.
- **Diffusion-controlled**: The energy storage is based on redox reaction due to the insertaion/extraction of electrolyte ions into/from electrode active material.

In the following sections these three charge storage mechanisms are described in detail.

1.2.1 Electric Double Layer Capacitor (EDLC) (non-faradaic)

EDLCs' charge storage mechanism refers to the electrostatic adsorption of the counterions at the surface of the charged nanostructure electrode. Consequently, the higher the specific surface area electrodes have, the larger the charge is possible to be stored. The nanostructure carbon base materials are known as the best choice for the electrode in EDLCs due to their low-cost manufacturing, abundancy, recyclability, and thermal stability. In addition, they show high capability in providing various nanostructures with a significant surface area. Activated carbon (the most popular carbon structures in ELDC), ordered mesoporous carbon (OMC), carbon nanotubes, and graphene composites are some of the common carbon structures. The EDLCs are characterized by their rectangular cyclic voltammetry (CV) and linear potential slope during charging/discharging vs. time in applying constant current. These properties are due to the instantaneous polarization of charges, which is possible in non-faradaic charge storage and the absence of ion diffusion [1, 8].
The capacitance can be evaluated through planar models if the electrode surface is the planar or cylindrical model if nanostructures (e.g., nanopores) are considered. The first planer model is the Helmholz model, where the counterions in the electrolyte solution are electrostatically absorbed in the pores' surface where the electrolyte behaves as a dielectric and makes the Helmholz layer figure 1.4(a):

$$C = \frac{\epsilon_r \epsilon_0 A}{d} \tag{1.1}$$

where ϵ_r is the electrolyte dielectric constant, ϵ_0 is the air permittivity, A is the electrode surface area, and d is the Helmholz plane layer thickness. Another planer model is the Gouy-Chapman-Stern model, which is more accurate, including stern and diffuse layers 1.4(b). However, the planar model may not be as accurate as the cylindrical model where the counterions insert into the pores:

$$C = \frac{\epsilon_r \epsilon_0 2\pi L}{b \quad ln(b/(b-d))} \tag{1.2}$$

where L in the pore length, b is the pore radius, and d is the dielectric thickness of the modeled capacitor. Figure 1.4(c) shows the cylendrical model of EDLC which is created on pores' wall [12].

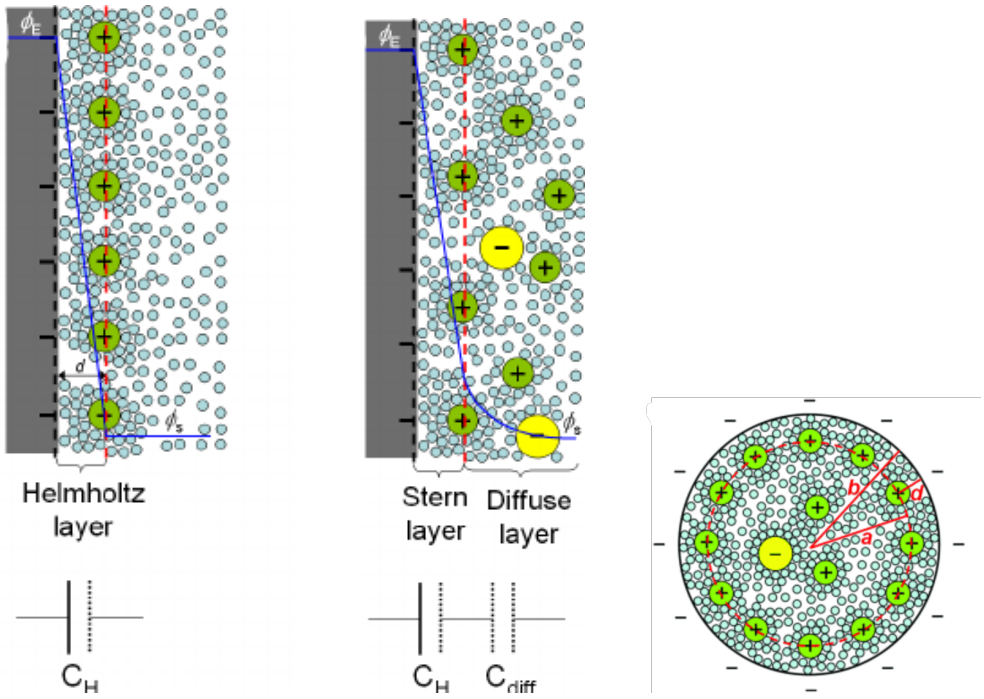

Figure 1.4: (a) Helmholz planer model (b) Gouy-Chapman-Stern model, and (c) cylindrical model of EDLC (here the positives iones insert into a pore of the negatively charged electrode and EDL is created). The green cycles are positive iones, yellow cycles are negative ions, and light-blue cycles are the electrolyte's solvent molecules [12]

1.2.2 Pseudocapacitance

Another type of EES device is pseudocapacitor that has characteristics more look-like to the EDLC. However, the storage mechanism is mostly based on electrochemical reactions related to the charge transfer process at the interface between the electrolyte and electrode, made with nanostructures. Consequently, this state-of-the-art technology has a higher charge storage level than EDLCs and overcomes the kinetic limitations (rate capability issues) that conventional batteries usually face. Figure 1.5 depicts the potential variation trend of the pseudocapacitors during the charging/discharging process and compares it with batteries and EDLCs. As shown in this figure, the potential variation is like neither batteries (constant) nor EDLC (linear with respect to the charge), but it can be located in the red zone between the battery-type and ELDC behaviour.

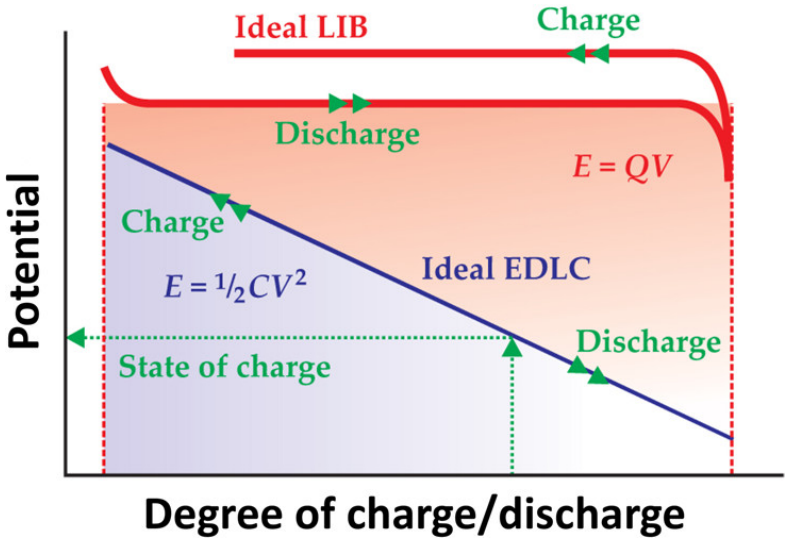

Figure 1.5: Potential-charge curve; comparison of different EES devices from ideal EDLC to ideal battery

The difference between batteries and pseudocapacitors is obvious when phase transformation is recognizable from the sharp peaks at different potential values during the charge/discharge process. Also, the plateau shape of potential in the galvanostatic charge/discharge curve (GCD) can be another phase transformation sign. During the chemical interaction in charge/discharge phases, the ion insertion into pores causes the strain of the material, leading to volume change and poor reversibility of the reaction. The equilibrium condition, which achievable from phase transformation, relaxes the strain of the structure. Consequently, the small phase transformation of pseudocapacitors, which can be observed from broad potential peaks and low potential differences of the reactions in charge and discharge stages in the potentiostat experiment proves the high life cycle and high rate capability of the pseudocapacitors in comparison with batteries [1].
According to the electrode material, the pseudocapacitors can be classified into three main categories: adsorption, redox, and intercalation pseudocapacitors. As shown in Figure 1.6, the intercalation and redox pseudocapacitors are identified by broadened peaks with very small phase transformation and rectangular shape in their CV curves, respectively.

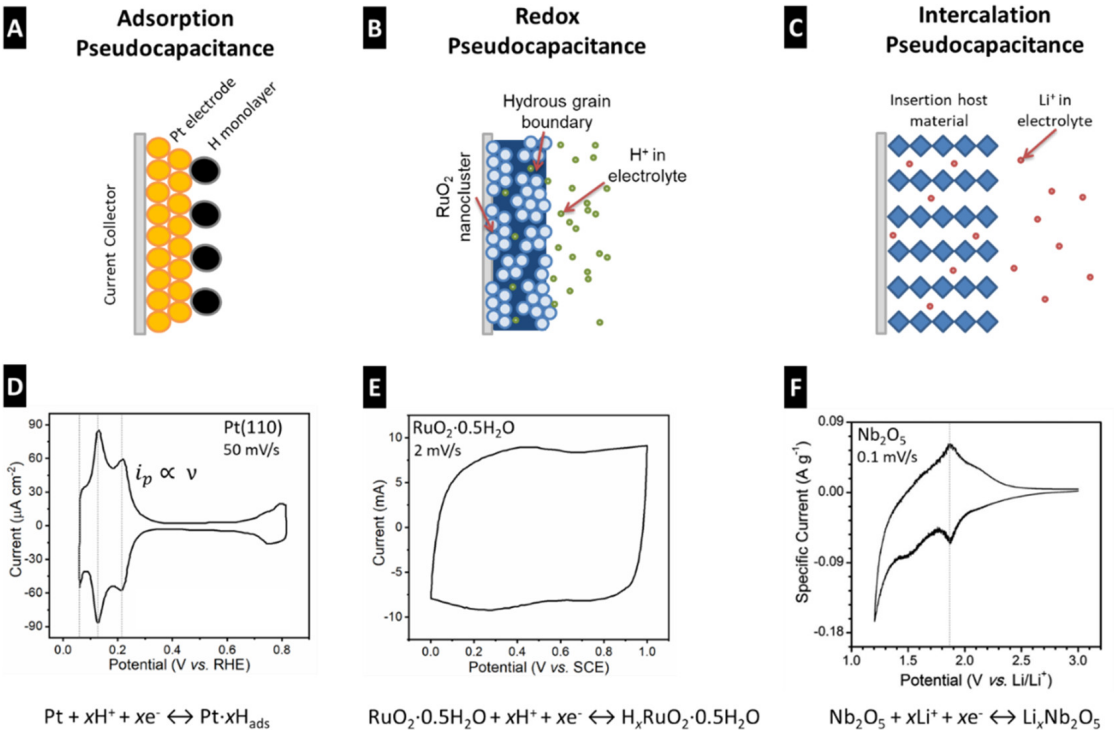

Figure 1.6: Different types of pseudocapacitors based on the active material structure with their typical CV curves (a) adsorption, (b) redox, (c) intercalation pseudocapacitance [13]

The typical chemical reaction in the negative electrode of the adsorption pseudocapacitance can be presented in the following:

$$M + A^+ + e^- \rightleftharpoons MA_{adsorption} \tag{1.3}$$

where M is the conductive active material covering the current collectors, and A^+ is the counterion inside the electrolyte, reacting with the electrons accumulated at the electrode.
The pseudocapacitors can also be categorized as extrinsic and intrinsic, which can be suitable to describe the lower diffusion limit in pseudocapacitors rather than batteries. In general, if the pseudocapacitive active material is made of thin films in order of nanometers, the diffusion length due to the mass transfer before the chemical reaction is significantly small compared to $\sqrt{D.\tau}$ (D is the diffusion coefficient and τ is diffusion time). However, as soon as the thickness of the material increases, a bulk (like crystalline structure)/nanostructure (like amorphous structure) layer over the electrode will grow, leading to the fabrication of extrinsic/intrinsic pseudocapacitor. As it is shown in Figure 1.7, the increase of the diffusion length in extrinsic pseudocapacitors results in the battery-like behavior

of these devices; in contrast, due to the high specific surface of the nanostructures electrodes in intrinsic devices, the CV curve mostly looks like the ELDCs [13].

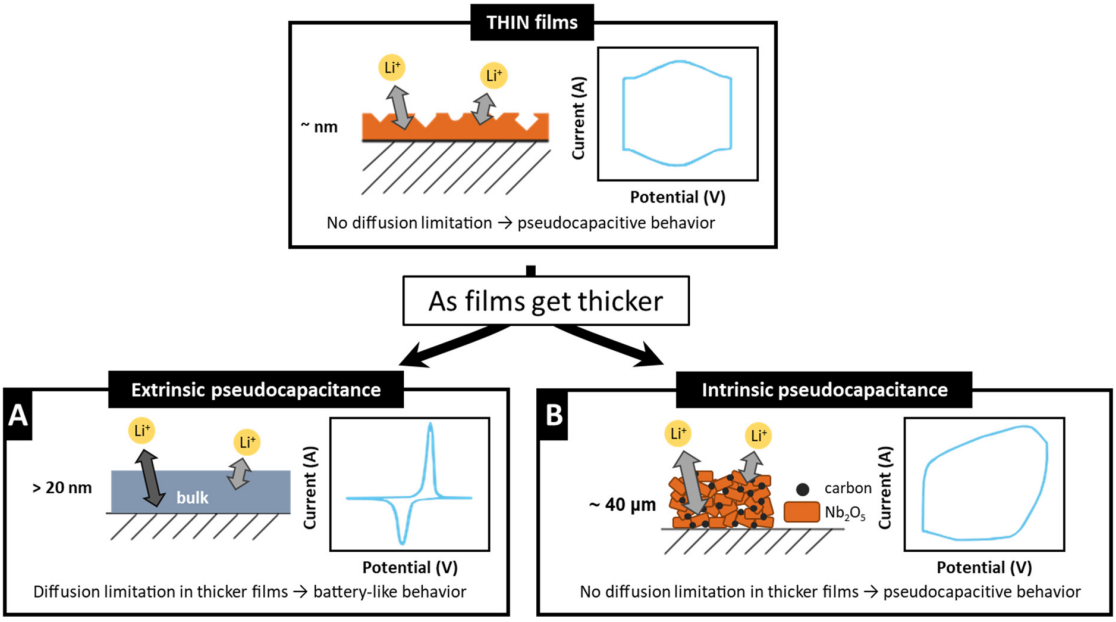

Figure 1.7: (a) extinsic and (b) intrinsic pseudocapacitance based on the thickness and crystalinity of the active material [13]

1.2.3 Diffusion controlled storage mechanism

The diffusion-controlled energy storage mechanism is associated with the redox reactions inside the electrode. Considering Li-ion batteries as an example, the redox reaction (insertion/extraction) of Li-ions at the anode results in the charging/discharging process. The difference between this mechanism and other ones appears in the sharp peaks and a plateau curve of the CV and GCD diagrams. That can be due to the phase transformation of the electrode during the charge and discharge process [2]. This faradaic mechanism can be observed in EES fabricated with a bulk electrode, usually crystalline insulators or semiconductors like metal oxides, where electron energy states are separated. As a consequence, the redox reactions take action at split energy levels (potential values) (figure 1.8). Putting aside the ohmic drop, which can cause the potential difference between anodic and cathodic peaks, the main reason for this peak-to-peak separation in reversible reactions can be found in the analyte diffusion and the electrode form (figure 1.1). Nevertheless, good conductivity or low energy state separation of material, or as shown in figure 1.8, the overlapping between the occupation bands, which is like the conjugated chemical bonds, can lead to redox peaks broadening. Consequently, the difference

between battery-like mechanism and pseudocapacitance can be recognized [14, 15].

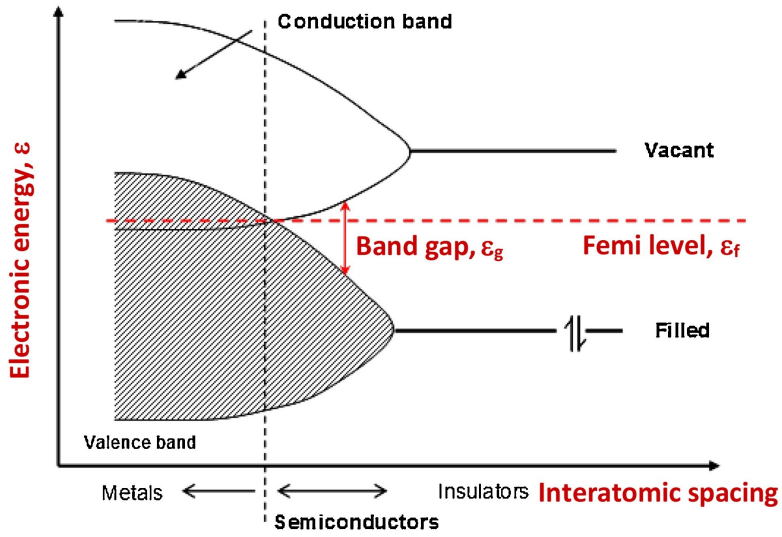

Figure 1.8: The energy band structure of different material [14]

1.2.4 From three-electrode measurements to device fabrication

In order to figure out whether the material electrochemical characterization is based on the non-faradaic or faradaic charge storage mechanism, a three electrochemical setup (half cell) is used, as shown in figure 1.9 (a). This setup contains a working electrode (WE), current collector, reference electrode (RE), and counter electrode (CE). The working electrode includes a thin layer of active material, coated over the current collector by a deposition method, such as the Dr. blade technique (figure 1.9 (b)) or automatic coating machines. The external current of electrons is generated between the counter electrode and the current collector, and the potential of the working electrode is measured with respect to the reference electrode.

Using three-electrode cells leads to recognizing whether the material is more proper for the negative electrode (anode) or the positive one (cathode) in an EES device. After selecting the proper choices for positive and negative electrodes, the packaging of an EES device is performed; figure 1.9 (c) shows a simple schematic of an EES device. Inside the electrochemical half/full cells, a thin layer of porous membrane structures, so-called separator, is used to prevent the electrical contact at the electrolyte between the electrodes [1].

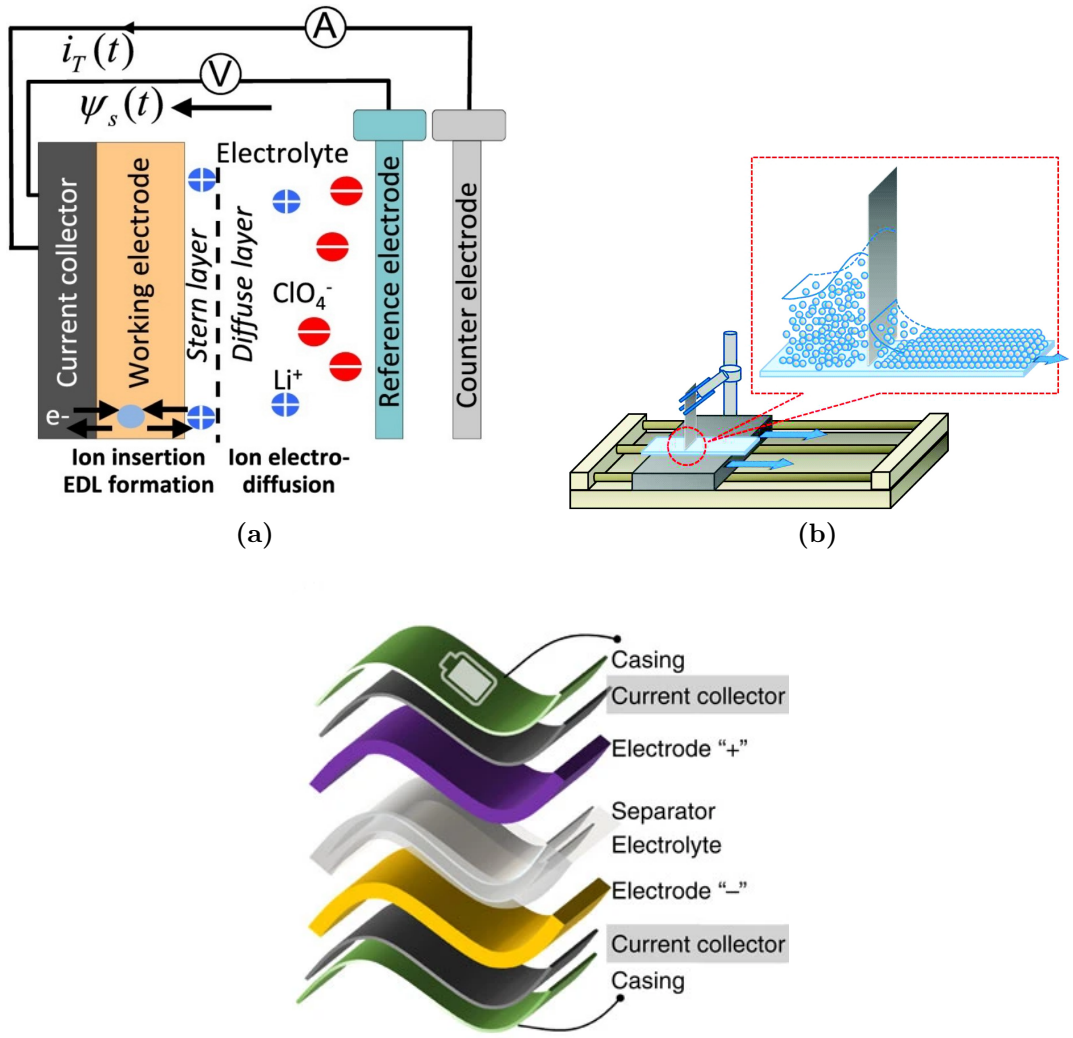

Figure 1.9: (a) An example of a three-electrode cell, containing $LiClO_4$ as the electrolyte [16], (b) Doctor Blade coating technique [17], and (c) The ingredients of a complete prepared package of EES device [1]

.

1.2.5 Overall charge storage and hybrid capacitors

An electrochemical energy storage (EES) device can be classified into symmetrical or asymmetrical devices, according to the charge storage mechanisms and the material of each electrode. Ideally, if the materials of the negative and positive electrodes are identical and have the same physical dimensions and mass, the EES

device is known as symmetric. Figure 1.10(a) presents an example of symmetrical quinone aqueous energy storage, made with alizarin-based electrodes [18], and figure 1.10(b) is the CV curve of symmetrical EDLC with porous carbon [19]. Although even if the two electrode materials are highly identical, due to the different sizes of anions and cations inside an electrolyte with respect to the electrodes, the CV curves and the EES device are not ideal symmetrical [1].

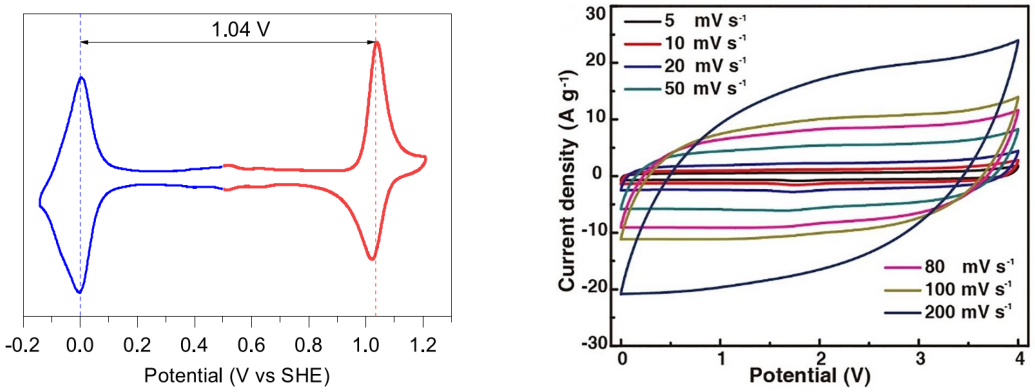

(a) **(b)**

Figure 1.10: Example of symmetric EES devices (a) Battery made with alizarin-based electrodes [18] (b) EDLC with porous carbon electrodes [19]

Asymmetrical EES devices contain positive and negative electrodes fabricated from two different materials. Utilization of this asymmetric structure, especially hybrid asymmetrical devices, not only leads to an increase in the operating voltage but also enhances the energy storage and rate capability thanks to an operation based on more than one electrochemical property on both electrodes. The large voltage range is achievable in a device involving anodic and cathodic materials at negative and positive electrodes. Considering both positive and negative electrode material with EDL charge storage mechanism, the total capacitance of EES devices is calculated as the following:

$$\frac{1}{C_{tot}} = \frac{1}{C_+} + \frac{1}{C_-} \tag{1.4}$$

where C_+ and C_- are corresponding capacitance of positive and negative electrodes. Also the total non-faradaic energy stored is:

$$E = \frac{1}{2} C_{tot} V^2 \tag{1.5}$$

where V is the operating potential window of the device.
The hybrid EES devices are usually based on both faradaic and non-faradaic charge

storage mechanisms. Figure 1.11 shows a comparison between the symmetrical and hybrid energy storage devices. Here, active carbon (AC) is the electrode of the symmetric devices and the positive electrode in the hybrid devices due to its high stability in the positive voltages in contrast to the metal oxide material (MeO), which is suitable for the anodes due to its stability in negative potentials. From figure 1.11(c), the faradaic charge storage mechanism can be qualitatively observed in the anode of the hybrid device and from the plateau curve of the negative charging potential with respect to the reference electrode (figure 1.11 (a)). Figures 1.11 (b) and (c) also compare the creation of EDL charge storage with the ion intercalation at the interface between electrode and electrolyte of two EES devices [1].

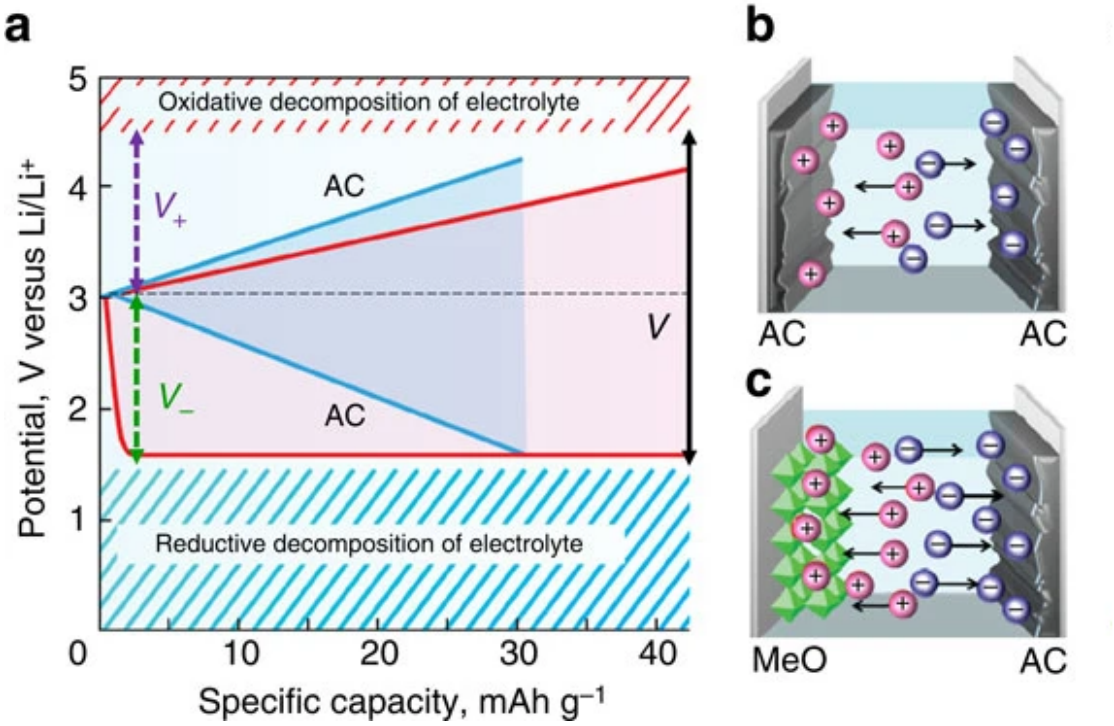

Figure 1.11: (a) Potential versus capacitance curve to compare symmetrical cell made by AC (blue line) and asymmetrical cell (red line), (b) symmetrical cell containing non-faradaic charging process, (c) assymetrical cell containing non-faradaic and faradaic charge storage mechanism on positive and negative electrodes, respectively [1]

In summary, the possible energy storage mechanisms of an EES device can be faradaic or non-faradaic. Additionally, depending on the application, whether a high power or high capacity device is targeted, different types of faradaic reactions can

be considered. Figure 1.12 shows a summary of the aforementioned different types of EES devices (faradaic or non-faradaic) by comparing their capacity, approximate charging duration, and structural variations due to the charging/discharging process.

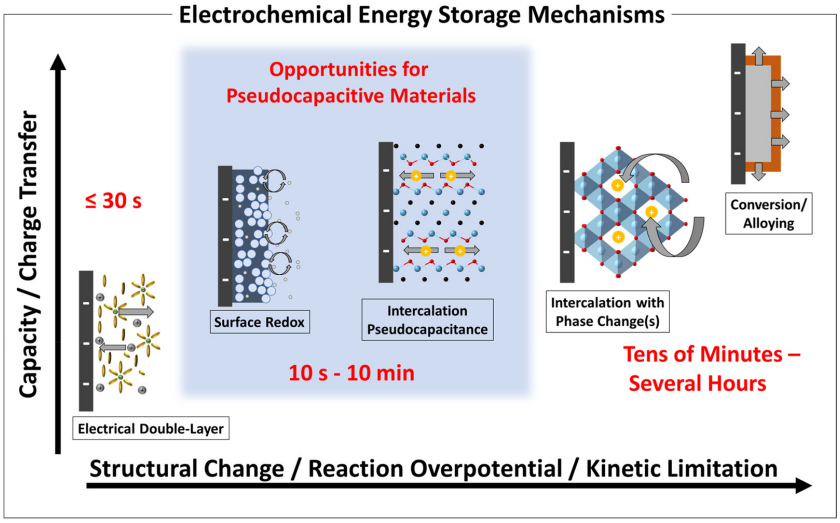

Figure 1.12: Categorizes of electrochemical energy storage mechanisms which are ordered based on the charging storage duration, the structural variation, and ion kinetic limits [13]

1.3 Performance evaluation of electrochemical cells

EES devices can be modeled through an electrical circuit, which can be found according to the active layer structure and charge storage mechanism. The simplest and most common electrical circuit is shown in figure 1.13. In a hybrid material based on both faradaic and non-faradaic charge storage mechanisms, the EDLC and pseudocapacitance are modeled separately by means of constant phase element (CPE), providing non-ideal capacitance. Evaluation of CPE is described in section 1.3.2 [20].
In figure 1.13, Rf, Ru, CPE_{dl}, and CPE_{pseudo} are charge transfer resistance, uncompensated series resistance, double-layer capacitance, and equivalent capacity of pseudocapacitance material, respectively.

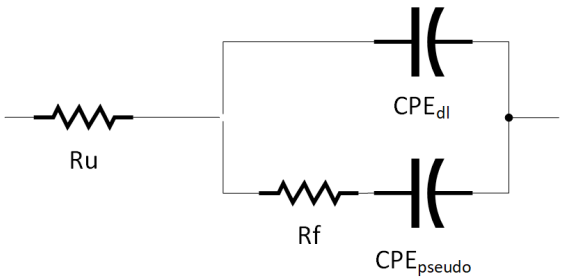

Figure 1.13: Equivalent electrical circuits of a half cell; considering pseudocapacitance and EDLC [20]

1.3.1 Equivalent resistances

The charge transfer resistance is related to the dopant or functional groups of carbon material at the surface of the electrode. In addition, this resistance, which is electrically parallel to EDLC, can be attributed to the faradaic reactions at the surface of pseudocapacitive material or the resistivity at the interface between the active material and current collector [21]. The series resistance of the equivalent circuit can be mainly related to the electrolyte ion transfer limitation and the ohmic loss in the interconnections of the electrical setup. In a full electrochemical cell, this resistance is called equivalent series resistance (ESR). The series resistivity can affect the power performance and energy efficiency of an EES device.
For the estimation of the resistances, the possible methods can be the electrochemical impedance spectroscopy method (EIS) in addition to the IR drop evaluation obtained from the CDG [11]. Both methods are discussed in section 2.3.

1.3.2 Capacitance

An EES device can be characterized by capacitance when the non-faradaic charge storage is relevant. The capacitance of an ideal EDLC can be evaluated trough the equation 1.6

$$C_E = \frac{Q_T}{\Delta V} \tag{1.6}$$

where Q_T is the total non-faradaic stored charge at the interface between an electrode and electrolyte and ΔV is the working potential range of the cell. According to figure 1.14, the total capacitance of a three-electrode setup (half cell) can be modeled by a single capacitor. In contrast, in a two-electrode setup (full cell), two EDLCs are modeled in series, and the total capacitance is evaluated by equation 1.4 [11].

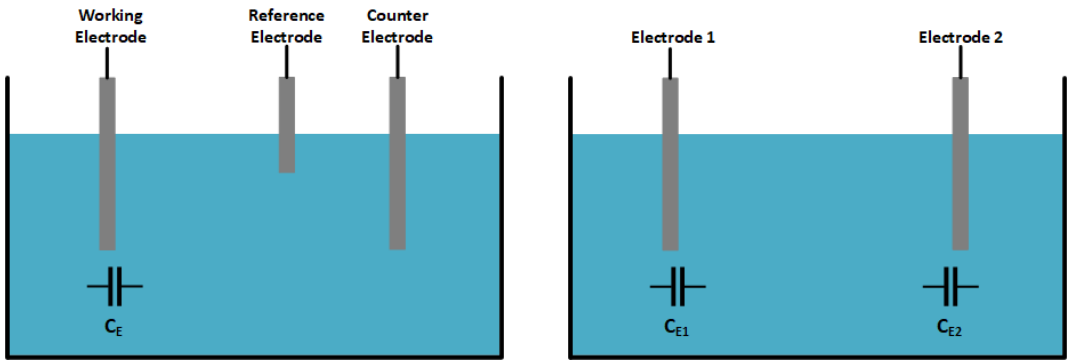

Figure 1.14: Capacitance model of (a) three-electrode, and (b) two electrode electrochemical cell

The capacitance can be evaluated through three different electrochemical characterization methods as the following:

- The integration of the CV curve leads to the evaluation of capacitance through the following equation:

$$C_T = \frac{Q_T}{\Delta V} = \frac{\int_0^{2V_0/\nu} |i| dt}{2V_0} \tag{1.7}$$

  where $V_0 = \Delta V/2$, ν is the scan rate, and i is the time dependent current. This integration is considered during the charging or discharging period.

- Through the galvanostatic charge/discharge method, the capacitance can be evaluated by the following formula:

$$C_T = \frac{I\Delta t}{\Delta V} \tag{1.8}$$

  where I is the constant applied current, and Δt is the duration of charge or discharge process.

- The capacitance can also be evaluated from the imaginary impedance, obtained from the EIS technique. The capacitance is usually evaluated by the impedance of the lowest measured frequency.

$$C_T = \frac{1}{2\pi f.im\{\mathcal{Z}\}} \tag{1.9}$$

It is worth mentioning that the specific capacitance is more common in the literature than the total capacitance.

$$C_S = \frac{C_T}{\Pi} \tag{1.10}$$

here Π can be the electrode volume, mass, or surface area. This parameter gives the researcher the possibility to compare their work with the others [11].

Constant Phase Element: CPE represents non-ideality of the capacitance in the equivalent electrical circuit (Figure 1.13). Consequently, the faradaic charge storage mechanism can be modeled by means of CPE (C_{pseud}) in pseudocapacitance materials.

$$Z_{CPE} = [(j\omega)^{\alpha} Q]^{-1} \tag{1.11}$$

where α and Q are frequency independent parameters and Q has capacitance units. $\alpha = 1$ is associated with an ideal capacitive behaviour, while $\alpha < 1$ corresponds to surface heterogeneity or the charge transfer reaction [13, 22].

1.3.3 Operating voltage

The operating potential window (PW) is an interval in which the electrochemical cell (three-electrode setup) works nominally. The electrolyte stability and the cell configuration (e.g., the type of electrode material or the symmetrical/non-symmetrical structure) are two main limiting factors defining the proper potential window. The stability potential intervals of aqueous electrolyte, organic solvent electrolyte, and ionic liquids are approximately 1 V, 2 V, and higher than 3 V, respectively. As a result, it is expected that EES devices with ionic liquid electrolyte provide a higher voltage window [11]. After evaluating the optimum potential window of a half cell through positively and negatively charging a half cell and selecting the suitable electrodes for anode and cathode of a full cell, the EES device is assembled. The operating voltage range of a device is obtained from the potential window of anode and cathode.
The coulombic efficiency is a standard figure of merit in defining the potential window.

$$\eta_{col} = \frac{Q^{-}}{Q^{+}} \tag{1.12}$$

Here Q^{+} is the total stored charges, and Q^{-} is the total released charges from EES. The closer coulombic efficiency to one, the higher stability of the EES is reached in a specific potential window.

1.4 Ordered mesoporous carbons and tungsten oxide electrodes for energy storage devices

The study of suitable anodic and cathodic materials is essential in order to reach an improved potential window in an asymmetrical EES device, which provides a

high capacity. As mentioned before, a hybrid EES device contains positive and negative electrodes with different materials. These hybrid structures can be based on the non-faradaic charge storage mechanism on the positive electrode and faradaic charge storage on the negative electrode or vice versa. Figure 1.15, obtained from [2], displays two different types of full hybrid cells. This project aims to improve the negative side of the potential window by proposing a carbon-based tungsten oxide compound as an anodic material; consequently, an EES hybrid device like figure 1.15(a) is interested. Ordered mesoporous carbon (OMC), as an active material with non-faradaic charge storage properties, is used as the electrodes of EDLCs. In this work, OMC is analyzed to increase the positive side of the potential window of a possible hybrid EES device in addition to the rate capability improvement.

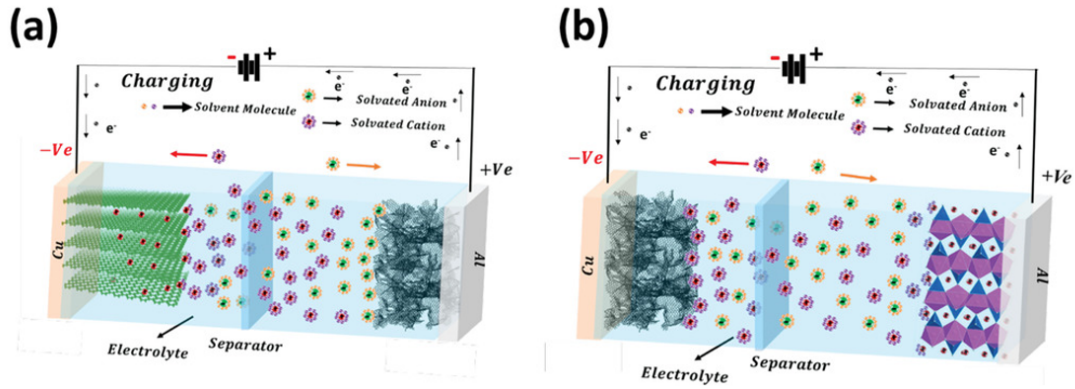

Figure 1.15: Two different hybrid electrochemical cells (a) pseudocapacitance as the anode and ELDC as the cathode (b) pseudocapacitance as the cathode and ELDC as the anode [2]

1.4.1 Cathode

Mesoporous carbon structures have been attracting attention in energy storage devices and electrocatalysts applications due to their electrochemical stability or low rate capacity of electrochemical reaction, high specific surface area, and pores volume. Owing to these advantages, they meet the high conductivity of electrons and ions compared to metal oxide materials, leading to high power energy storage due to the creation of EDLC. These materials can be classified into ordered and disordered structures with regular and irregular pore arrangements, respectively. Additionally, the porous carbon materials are classified as micropores, mesoporous, and macropores when the diameter is lower than 2 nm, between 2 and 50 nm, and higher than 50nm, respectively [23, 24]. In this work, we focus on ordered mesoporous carbon (OMC) as the positive electrode. Consequently, the non-faradaic charge storage mechanism at the OMC interface of the cathode is interested.

1.4.2 Anode

Tungsten oxide nanostructures are popular materials utilized as anode due to their large potential window in the negative charging, their low cost, the tunnel structure facilitating the ion insertion, and thermal stability. Moreover, offering both faradaic and non-faradaic charge storage mechanisms in tungsten oxide electrodes leads to a trade-off between the rate capability and energy density. The low-cost electrode preparation, such as Dr. Blade's technique, is another advantage of using these materials. On the other side, the lower operating power compared to carbon-based supercapacitors and poor conductivity are the most significant drawbacks of tungsten oxide. Using tungsten oxide composites and controlling the pore size by modifying the crystallinity can alleviate the mentioned issues [25].

Tungsten oxide crystal structure

Tungsten oxide compounds can be categorized into stoichiometric (WO_3) and non-stoichiometric (WO_{3-x} 2<x<3). Depending on the thermal treatment, the tungsten oxide compound can have various crystal structures, such as monoclinic, triclinic, tetragonal, orthorhombic, cubic, and hexagonal.

- **Stoichiometric (WO_3)** can be categorized as a polymorphs material, depending on the temperature. Basically, the WO_3 includes a tungsten atom as cation surrounded by six oxygen atoms leads to a corner-sharing WO_6 octohedra as displayed in figure 1.16 (a). However, due to WO_6 displacement in different temperature, one of the following polymorphic forms can be obtained: tetragonal ($\alpha - WO_3 > 740^oC$), orthorhombic ($\beta - WO_3$, $330 - 740^oC$) (figure 1.16(c)), monoclinic I ($\gamma - WO_3$, $17 - 330^oC$) (figure 1.16(b)), triclinic ($\delta - WO_3$, $-43 - 17^oC$), and monoclinic II ($\epsilon - WO_3$, $> -43^oC$) [6].
  Additionally, as figure 1.17 shows, an interesting hexagonal tunnel structure is generated, leading to improve the positive ion insertion through the active material and, consequently, increasing the rate capability of EES devices. As a result, this hexagonal structure has become a promising anode material in Li-ion batteries [26, 27].

- **Nonstoichiometric WO_x (x=2.625-2.91)** is specified due to the oxygen decrease compared with stoichiometric tungsten oxide (WO_3). The increase of oxygen vacancies results in the corner-sharing arrangement of WO_6 octahedra turns to edge-sharing. The different crystal structures, including orthorhombic, monoclinic, and tetragonal, are called Magneli phases, which can be obtained by reducing the monoclinic structure of stochiometric WO_3. The nonstoichiometric WO_x has become popular materials due to the oxygen vacancies at the

surface, leading to improved absorption affinity and conductivity and bandgap reduction [6].

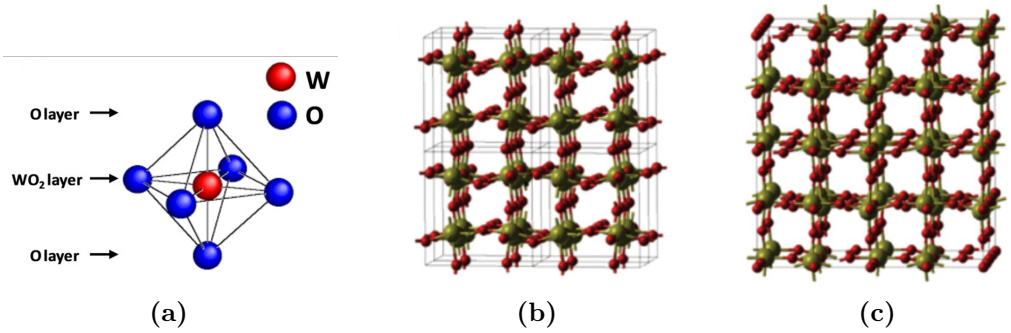

Figure 1.16: (a) WO_6 octahedra leading to corner sharing structures (b) room temperature monoclinic structure, and (c) orthorhombic structure; here the red spheres are W and green ones are O atoms [6]

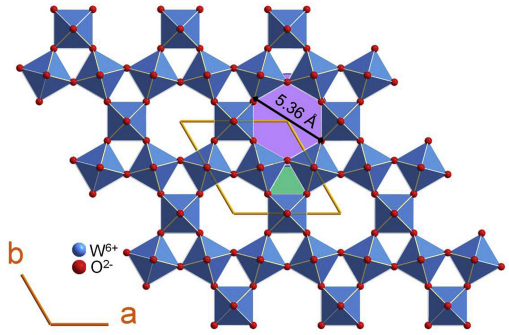

Figure 1.17: $h-WO_3$ structure, the hexagonal and triangular tunnels are specified here [27]

Tungsten stability in aqueous solution (pourbaix diagram)

Tungsten owns a wide range of oxidation states from -2 to +6; thus, the study of its stability in an aqueous solution is essential in order to select a proper electrolyte for the electrochemical cell. The dependency of metal or metal oxide on the pH value of the electrolyte is studied by means of a half-cell reaction, which leads to preparing the Pourbaix phase diagram. Generally, the Pourbaix diagram represents the oxidation-reduction reactions in a half-cell in equilibrium condition; besides, it displays the electrochemical potential, which is the energy needed for oxidation reaction, versus the pH of the electrolyte. According to the Pourbaix

diagram of tungsten in figure 1.18, tungsten can passivate to different oxide forms in an acidic electrolyte with $pH < 4$, while among them, only WO_2 and WO_3 are thermodynamically stable in nature. As this figure presents, the tungsten oxide passivation, which leads to WO_3 production, is not possible for $pH > 4$. As a result, utilizing the electrolyte with $pH > 4$ can result in the corrosion of WO_3 electrode [6].

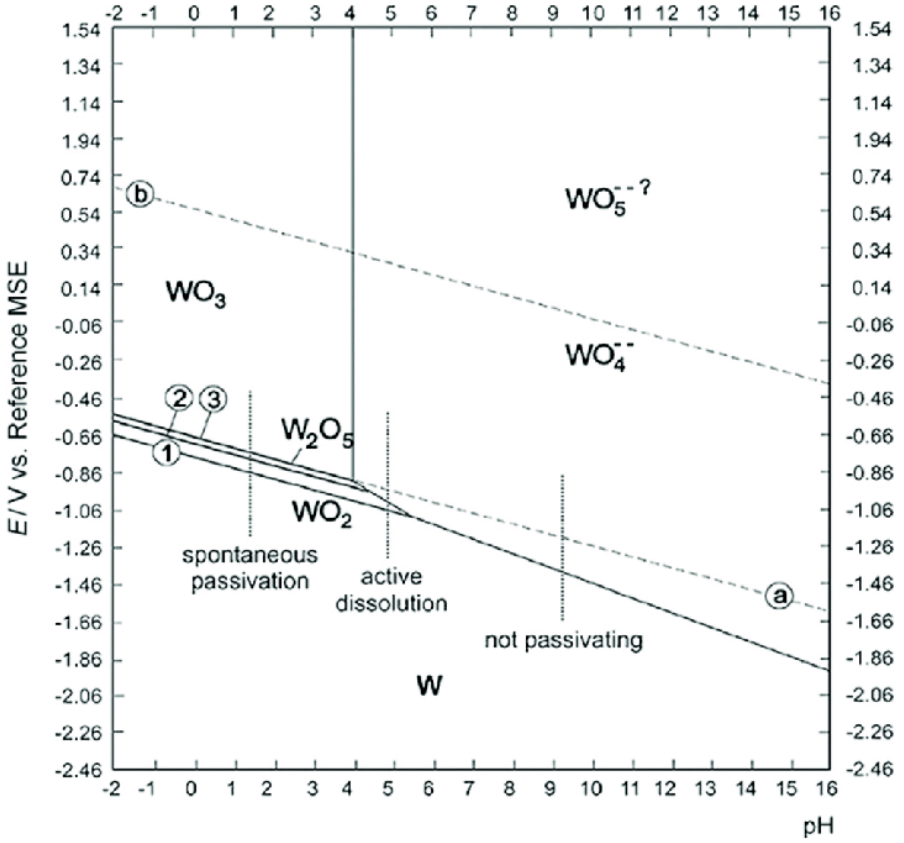

Figure 1.18: Pourbaix diagram of Tungsten [28]

WO_x - Carbon composite

One possible approach to enhance electrochemical performance and increase the conductivity and specific area of WO_x materials is utilizing hybrid WO_x - carbon structures. Additionally, tuning the structure and size of carbon materials can affect the electrochemical properties of a cell containing this hybrid material as the electrode. As a result, both faradaic and non-faradaic charge storage mechanisms can be expected in these composites [6]. In this project, the $OMC - WO_x$ hybrid materials are studied as the anode electrode of EES. Consequently, the enhancement of the operating potential window on the negative side compared to the OMC

electrode is expected, which leads to the improvement of the cell's capacity.

1.5 Liquid electrolytes

The electrolyte material is a critical element, defining the performance of electrochemical energy storage (EES). The possible figure of merits for choosing the electrolyte solution can be the high conductivity of ions (e.g., low viscosity), large electrochemical stability window, low cost, low environmental impact, and high-temperature stability. Considering ions that composed the salt material dissolved in a solvent in a liquid electrolyte, their conductivity and chemical adsorption inside the active material are essential to reach a higher rate capability and high specific energy. In addition, the salt must completely dissociate inside the solvent [29].
Consequently, the study of different electrolytes and comparing electrochemical characteristics of fabricated energy storage are essential for EES device manufacturing. In the following section, the chemical characteristics of the water-based and organic liquid electrolytes are discussed.

1.5.1 Water-based electrolytes

Aqueous electrolytes are popular in energy storage devices due to their low cost and low environmental impact. Their main drawback is the low operating potential window (<1.23 V), limited by the O_2 and H_2 evolution, as shown in eq. 1.13 and 1.14, respectively

$$2H_2O \rightarrow O_2 + 4H^+ + 4e^- \tag{1.13}$$

$$2H^+ + 2e^- \rightarrow H_2 \tag{1.14}$$

In figure 1.19, the Pourbaix diagram of water is displayed where the potential values are considered versus the standard hydrogen electrode (SHE). In this work, the water-based electrochemical cell is fabricated, which involves sulfuric acid (H_2SO_4) solution as its electrolyte. The anode charging and discharging process is related to the H^+-ions adsorption at the interface between the electrode and electrolyte, while the negative ions (SO_4^{2-} in this case) participate in the charging process at the cathode and electrolyte interface. The low viscosity of water-based electrolytes leads to higher conductivity of the ions inside the solution compared with organic electrolytes, which positively affects the charging process by improving the rate capability of the cell [3].

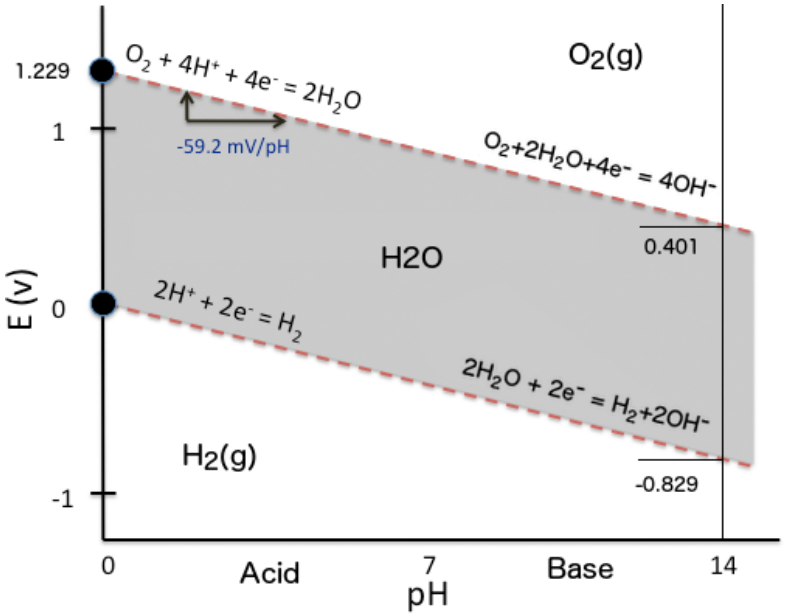

Figure 1.19: Pourbaix diagram of water [30]

1.5.2 Organic solvent electrolyte

The main advantage of organic electrolytes is the larger operating voltage (<2.7 V) than water-based electrolytes, thanks to the formation of the Solid Electrolyte Interface (SEI) layer from the decomposition in the first scan of Li-based electrolyte. However, large viscosity, inflammability, environmental effects, and low ion conductivity, especially in low temperatures, are the main disadvantages of these types of electrolytes.
According to the mentioned figure of merits in choosing the electrolyte, several organic solvents are investigated in EES manufacturing based on the application. The conventional and basic organic solvents are linear or cyclic carbonates, such as Ethyl Methyl carbonate (EMC), dimethyl carbonate (DMC), propylene carbonate (PC), and ethylene carbonate (EC). However, in the recent technologies, in order to enhance the electrolyte performance, by achieving low viscosity, high ability in the formation of the SEI layer, and high dielectric constant (essential to dissolve the salt properly), the mixture of cyclic and linear carbonate organic materials can be helpful. As a common mixture, utilizing EC and DMC together, with 1:1 proportion, gives us high dielectric constant thanks to EC and low viscosity thanks to DMC. The utilized salt must contain Li^+ as cations in the Li-ion based energy storages. The possible anions for the Li-based salt can be ClO_4^-, BF_4^-, AsF_6^-, $TFSI^-$, and PF_6^-. Among these salts, $LiPF_6$ is the most popular and suitable salt for organic solvent, as it meets the considered figures of merit of a suitable

electrolyte [29].

1.6 Thesis outline and goals

1.6.1 Material synthesis

The desired materials in this project are ordered mesoporous carbon in addition to the composition of OMC and WO_3 ($OMC - WO_3$). Firstly, the synthesis procedure of both materials is described. Later on, by performing thermal annealing, three different samples of $OMC - WO_3$ are prepared; so that its impact on physicochemical properties of material and electrochemical properties of energy storage cells would be analyzed in the following steps.

1.6.2 Physicochemical properties of OMC and $OMC-WO_3$

There are three investigated techniques for figuring out the physicochemical properties, including X-ray diffraction (XRD), field emission scanning electron microscopy (FESEM), and energy-dispersive X-ray spectroscopy (EDX). Short descriptions of these methods are provided in the second chapter. Later, the synthesized materials' physicochemical properties are given in the third chapter, where the results obtained from these three methods are given.

1.6.3 Energy storage properties of OMC and $OMC - WO_x$

This project is based on the characterization analysis of aqueous and aprotic (coin cell) half-cells. The electrochemical properties of the assembled cells are discussed in the third chapter. CV, GCD, and EIS are the considered methods for electrochemical characterization. The descriptions of these methods are given in the second chapter. The potential window in which a high coulombic efficiency can be reached, rate capability, specific capacity, and stability of each cell are the electrochemical properties that would be analyzed in the following.

1.6.4 Determination of the charge storage mechanisms in different electrolyte

The critical aspect in classifying energy storage is the identification of storage mechanisms. This can lead us to monitor the rate capability and capacity of the fabricated cell. As it was mentioned previously, the storage mechanism can be either faradaic or non-faradaic (or EDL). The first mechanism belongs to the surface-controlled charge storage contribution, while the latter one might be surface

or diffusion controlled. Additionally, the reversibility of faradaic storage mechanisms (redox reactions) is an essential aspect. These classifications of the fabricated cells would be discussed in the third chapter as well.

1.6.5 Determination of the diffusion coefficient of the cation insertion/extraction (Li^+)

This project's final investigation is analyzing the Li-ion diffusivity into/from the amorphous materials within the charging/discharging process. Consequently, the diffusion coefficient is evaluated through the Galvanostatic Intermittent Titration Technique (GITT) in order to analyze the diffusion-controlled storage.

Chapter 2

Methods and materials

2.1 Instruments

2.1.1 Electrochemical workstations

Potentiostat

The electrochemical half cell can be modeled as an electrical circuit, shown in figure 2.1.

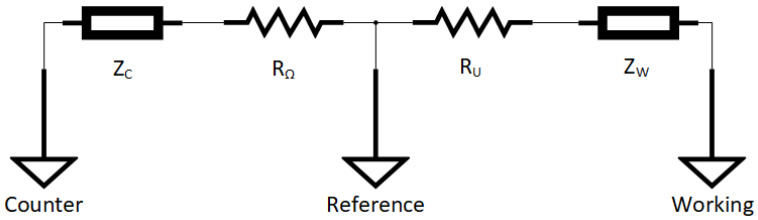

Figure 2.1: Equivalent impedance network of an electrochemical half cell

Here, the resistors model the voltage drop across the solution, which is known as a non-ideal parameter affecting the controlling voltage of the system. The energy storage mechanism of the cell at the electrode interface is modeled by the impedance parameters (Z_C, Z_W). The potential of the whole system is measured with respect to the reference node (electrode).
There can be several potentiostat instrumental designs, depending on the potentiostat experiment (e.g., CV). The following circuit (figure 2.2) is known as the fundamental model that owns the basic principle of the half cell's controlling system. In figure 2.2, e_i is the applied voltage to the potentiostat system. As an example, in the CV experiment, e_i is a sweep potential, which is variable by time [31]. In the potentiostat system, the potential between reference and working

electrodes is controlled by the user; besides, the potential between the counter and working electrode and the current flow from counter to working electrode should be monitored [32].

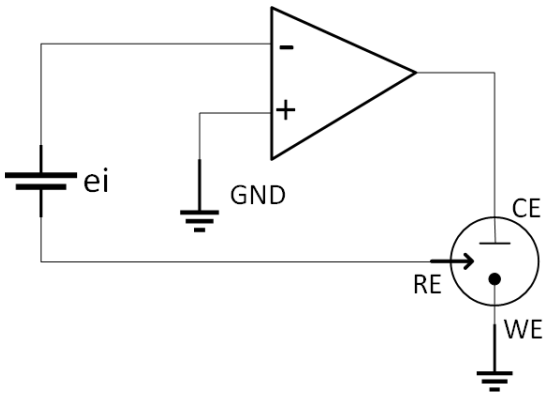

Figure 2.2: Equivalent circuit for potentiostat instrumental design

Galvanostat

The galvanostat setup is based on the current controlling system, such as the GCD technique and GITT; in the former technique, a constant current is applied, and in the latter one, a periodic pulse current is applied. A fundamental galvanostat setup is shown in figure 2.3. Here, the current flow from the counter electrode to the working electrode (= current across the resistor R) is controlled, which can be modified by the applied voltage, e_i, (eq. 2.1). The working electrode potential with respect to the reference electrode is monitored [31, 32].

$$i_{cell} = \frac{-e_i}{R} \tag{2.1}$$

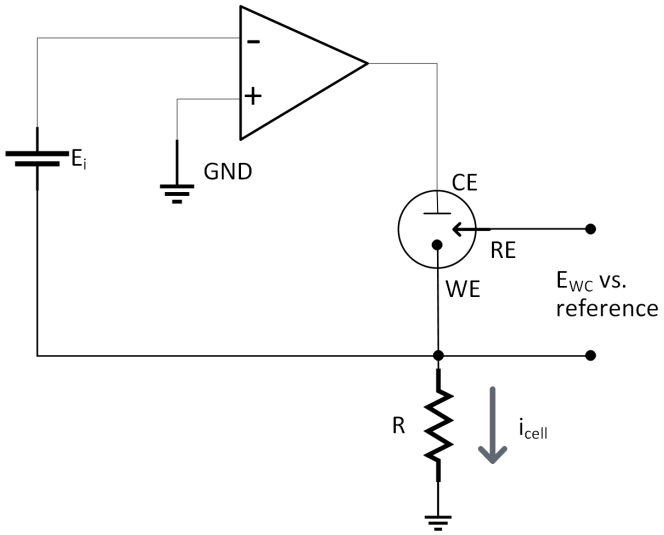

Figure 2.3: Equivalent circuit for galvanostat instrumental design

2.1.2 Physico-chemical characterization

X-ray Diffraction (XRD) analysis

Crystalline structures contain a regular and periodic arrangement of atoms or ions. A constant distance separates each plane of atoms from the other planes. This distance is identical for each crystal, which is its main characteristic feature. XRD is an experimental method to analyze the crystallinity level of a sample in addition to measuring the atomic distance of crystal material, which helps identify the crystal composition of a sample. X-rays are electromagnetic radiations oscillating in periodic cycles, and the electric and magnetic waves are perpendicular to each other and the propagation direction. Their wavelength range is from $10^{-}3$ to 10 nm. There is the propagation of X-rays with a constant wavelength, λ_0, over the desired material in the XRD technique. Due to the periodic structure of crystals, the X-rays are scattered from the surface of the material in specific incident angles (figure 2.4). This phenomenon is known as Bragg's law follows equation 2.2.

$$n\lambda = 2dsin\theta \tag{2.2}$$

where n is the order number and d is the distance between each crystal plane in the periodic structure. By assuming constant wavelength, the scattering angle can be obtained in the XRD measurement. According to the several order number of scattering, the XRD plot can be observed with more than one peak.

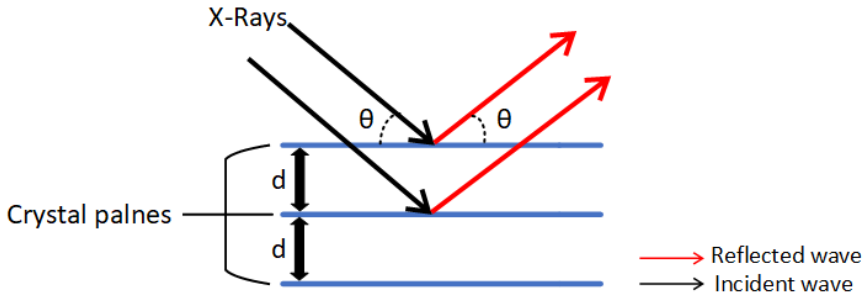

Figure 2.4: The rays scattering (reflection) in the critical angle from the surface of the periodic structure of a crystalline material according to the Bragg's law

Usually, in the XRD experiment, a mass of crystalline powder is desired to be analyzed, which is constructed by several crystals located randomly across every possible axis with respect to the incident angle of X-rays. As a result, a large number of diffraction is expected in each incident angle. A photographic film or plane is used as a detector of the diffracted rays leading to calculating the desired sample's critical angle. As shown in figure 2.5 (a), a diffraction-cone is created, leading to observe a cycle of the diffracted rays in the detector. Consequently, the critical angle can be evaluated by equation 2.3.

$$\frac{L}{2\pi R} = \frac{2\theta}{360} \tag{2.3}$$

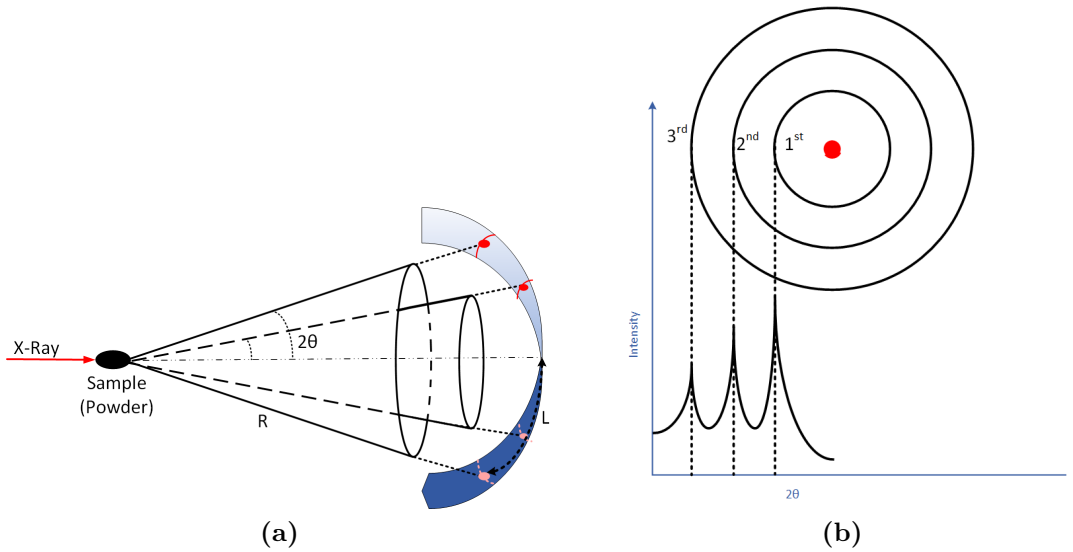

Figure 2.5: (a) XRD measurement for a powder sample (b) An example of the XRD test result

According to figure 2.5 (a), if we imagine a circular form for the detector whose center is aligned with the sample position, the constant radius of this circle (R) can be considered the distance between the detector and the sample. Each circle illustrated at the detector in the XRD test belongs to an order number. As a result, several peaks can be obtained in the final XRD plot, as shown in figure 2.5 (b) [33, 34].

Field Emission Scanning Electron Microscope (FESEM)

Concerning the nano/micro scale of materials used in this thesis, magnification of their image through the convectional optical microscopic approaches and devices is impossible due to their low dimension in comparison with the visible light. Consequently, the scanning electron microscope (SEM) is used to magnify the picture of materials up to 300,000 times. The electron beam, which is usually created by a field emission gun (FEG), is emitted over the sample after passing through a focusing lens. The working principle is based on the detection of the electron beam (electron detection) scattered from the material's surface after performing a regular scanning pattern. The schematic of FESEM layout is illustrated in figure 2.6 [35].

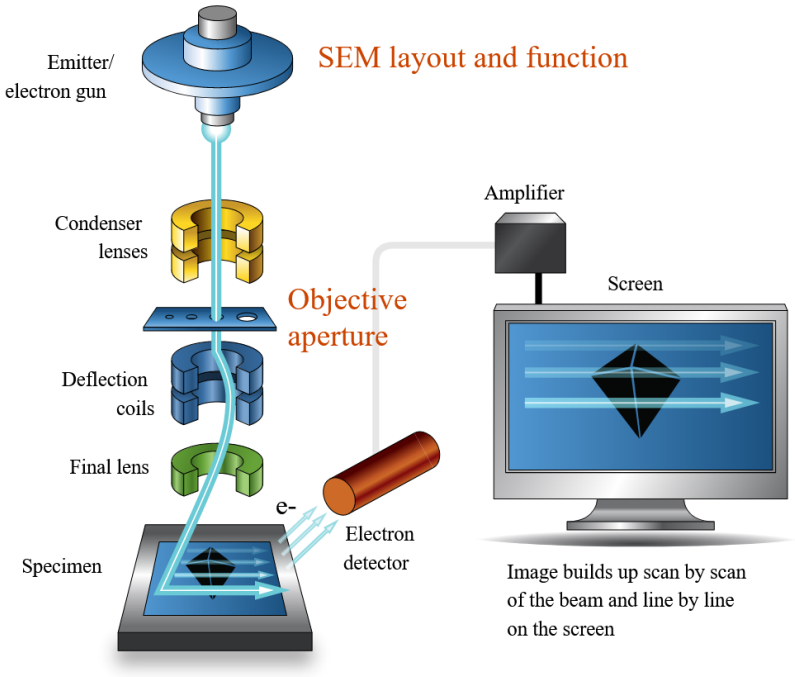

Figure 2.6: The basic layout of SEM [35]

2.1.3 Energy-Dispersive X-ray Spectroscopy (EDX)

Energy-Dispersive X-ray Spectroscopy (EDX) is another physicochemical characterization method to identify the elements present inside a sample and their proportional concentration. In this method, high energy beams, such as high energy electron beams or X-rays, are applied through a sample, leading to the excitation of core electrons in each atom. Subsequently, the outer shell electrons transit into the lower energy levels to fill the unoccupied energy levels at the inner shells, which leads to an identical X-ray emission for each element. Consequently, the elements can be defined based on the obtained spectrum with respect to the energy (or wavelength) of each emitted ray [36].

2.2 Materials

2.2.1 Reagents

Ordered Mesoporous Carbon (OMC)

As mentioned in section 1.4.2, OMC is a common mesoporous structure proposing EDLC specification and commonly used as the cathode material in hybrid EES devices. By considering an electrochemical cell containing OMC as the positive electrode, the negative ions inside the electrolyte are attracted by this electrode within the charging process. Subsequently, the EDLC is created at the surface of the cathode [37, 38]. In this work, OMC is used as the active material of the working electrode in a three-electrode setup. This would lead us to evaluate the possibility of selecting OMC as the positive electrode of an EES device. Additionally, a hybrid composition of metal oxide/carbon-based material is synthesized, which can be used as the anode of an EES device. We expect an enhancement in the energy storage and specific power thanks to the introduced hybrid material.

Tungsten Oxide (WO_3)

The main investigated material of this project is the carbon-tungsten oxide composite. The wide range of tungsten oxide potential widow in the lower potential values with respect to the reference electrode would make it a proper choice as an anode in an EES device. Besides, this hybrid material's carbon composition is anticipated to provide a high surface for the active electrode enhancing the rate capability in the charging/discharging process. It is worth mentioning that the tungsten oxide material in this project is assumed to be stoichiometric (WO_3) (section 1.4.2).

Electrolyte

In the first part of this project, a water-based solution, including 0.5 M sulfuric acid (H_2SO_4), degassed with N_2, is used as the electrolyte of half cells. Later, an aprotic electrolyte including $LiPF_6$ as the solute and EC:DMC (1:1) mixture, as the solvent, are utilized for preparing a Li-ion-based half coin cells.

2.2.2 Hydrothermal synthesis microwave

Ordered Mesoporous Carbon (OMC)

Hexagonal mesoporous silica, SBA-15, is used as the hard template in the preparation of OMC. The first step is SBA-15 preparation; 5 g Pluronic P123 (triblock copolymer), as the surfactant tetraethylorthosilicate, is dissolved into a solution of water (170 mL) and HCl (24.7 mL), at 40 ^oC. Later, as the silica source, 12 mL of TEOS (tetraethylorthosilicate) is added at the same temperature. After 24 hours of continuous stirring of the solution, it is put in the oven for 24 h at 100 ^oC. The obtained mixture is filtered and washed throughly with water. After drying in oven, the powder sample is calcined for 10 hours at 550 ^oC under air to remove the surfactants [39].

The template method is used to obtain OMC through the carbonization of sucrose into SBA-15 and later on removing the template (SBA-15). This method provides flexibility to control the morphology and size of pores, in addition to the simple synthesizing procedure. Firstly, a solution containing sucrose, sulphuric acid, and distilled water with amounts of 1.25 g, 0.14 g, and 5.0 g, respectively is added to 1 g of SBA-15. The obtained mixture is heated at 100 ^oC for 6 hours and later at 160 ^oC for another 6 hours. Subsequently, the internal pores of SBA-15 silica are infiltrated with carbon precursor by adding 0.8 g of sucrose, 0.09 g of H_2SO_4, and 5.0 g of H_2O, and then the same thermal treatment proceeds. Later, the pyrolysis under nitrogen flow is performed at 900 ^oC for 6 hours to carbonize sucrose. Finally, in order to reach the final mesoporous structure of carbon, the silica is removed by washing the composition in 2 M NaOH solution (50% H_2O + 50 % ethanol) overnight at room temperature [40].

Hybrid material $OMC - WO_3$

For synthesizing the hybrid material, 1 gr of OMC is added to 50 ml of Phosphotungstic acid (PWA) aqueous solution. The suspension is left at room temperature for 72 h under continuous stirring. After filtering and drying the obtained black powder at 80 ^oC in 6 hours, the thermal annealing under N_2 flow at 300 ^oC and 400 ^oC, 600 ^oC is performed to prepare three different samples. As a result, the OMC layer's decoration with WO_3 particles acheived from the absorbed PWA (the

proportion of OMC to WO_3 is 70% to 30%) [40]. The transportation of protons from PWA to the carbon material is the fundamental factor leading to prepare these hybrid materials [41, 42, 43]. The temperature affects the crystallinity level of the hybrid material, and subsequently, the impact of this difference on the electrochemical characteristics is the case of study in this project.
The four samples analyzed in this study are called OMC, $OMC - WO_3 - 300$, $OMC - WO_3 - 400$, and $OMC - WO_3 - 600$.

2.2.3 Electrochemical cells assembly

Aqueous Cell

The water-based cell is assembled based on a three-electrode galvanic cell (figure 1.14 (a)). In order to prepare the working electrode ink, 2 mg of the prepared mixture of active materials is added to a mixture of 50 ul H_2O, 50 ul Isopropyl Alcohol (IPA), and 15 ul Nafion 5% as the binder and sonicated to reach a homogeneous ink. The synthesized inks (OMC, $OMC - WO_3 - 300$, $OMC - WO_3 - 400$) are coated over a glassy carbon electrode (GC) (circular surface with 0.076 cm^2 area) as the current collector applying the dr. Blade's technique so that the working electrode with 0.54 mg/cm^2 mass loading is prepared. The counter and reference electrodes are made by Pt wire and Ag/AgCl, which included 3 M NaCl, respectively. Within the charging/discharging process, the electrolyte is purged via N_2 to remove the oxygen molecules. 0.5 M sulfuric acid (H_2SO_4) is the aqueous solution considered as the electrolyte here. Additionally, the mass loading of the active material and the surface area of WE are equal to 0.5 mg/cm^2 and 0.076 cm^2, respectively, which are identical for all fabricated cells.

Coin cell made by aprotic electrolyte

Before assembling the electrochemical cells, the desired ink is prepared made by the following ingredients: a mixture of 75 % of OMC or $OMC - WO_3$, 10 % of carbon black (CB), and 15 % Polyvinylidene Fluoride (PVDF). CB is used as the conductive additive in order to improve the conductivity of the working electrode [44, 45]. PVDF is used as the binder due to the polymer chains' electrochemical stability in contact with the electrolyte and high elasticity. [46, 47, 48].
The coin cell is the desired structure to implement the aprotic electrochemical half-cell. The prepared ink (active material) is coated over an aluminum current collector via Dr. Blade's technique. The current collector diameter and mass are 15 mm and 7.7 mg, respectively. Consequently, the total mass and the mass loading (g/m^2) of the active material can be calculated after measuring the total mass of the working electrode. The Whatman membrane is used as the separator, located inside the Li-ion-based electrolyte with 1 M $LiPF_6$ in EC:DMC solvent.

The RE/CE, as a single electrode in the coin cell, is Li-metal. The coin cell is assembled as shown in figure 2.7 and like what is described in [49, 50].

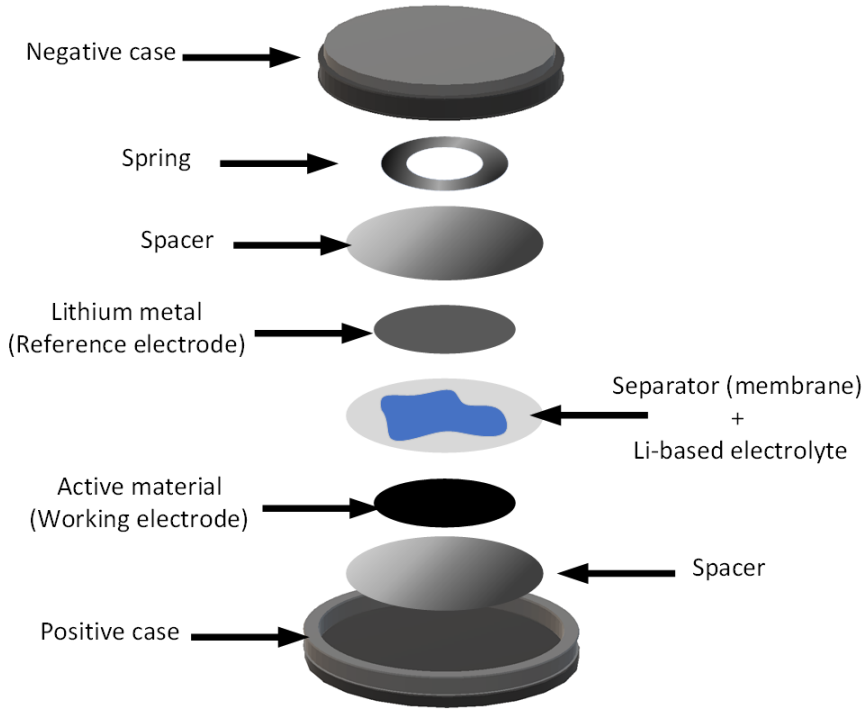

Figure 2.7: Assembling process of a coin cell (half-cell)

2.3 Methods: Electrochemical characterization

2.3.1 AC impedance spectroscopy

Electrochemical Impedance Spectroscopy (EIS) is a powerful technique to perform the charge transfer and storage analysis of an electrochemical cell. Figuring out the type of interfacial reaction in different frequencies leads to model equivalent electrical capacitive elements for each reaction mechanism. Besides, the resistive factors, including the series resistance and charge transfer resistance, can also be modeled (figure 1.13). In this method, a small sinusoidal signal is applied over the cell with a given DC bias, and frequency range [51]. Two types of figure are common to display the impedance data:

1. **Bode plot** displays the impedance magnitude and phase with respect to the frequency.

2. **Nyquist plot** provides the relation between the real impedance on the x-axis and the imaginary one on the y-axis. According to this plot, the series resistance of the device can be evaluated in high frequencies when the imaginary impedance is zero. This resistance models mainly the electrolyte ion conductivity and electron transmission across the electrical components of the cell. The presence of semicircle in high frequencies account for the interfacial reaction, which can be modeled by a parallel RC circuit in which R can be due to charge transfer (faradaic reaction) or interfacial impedance (impedance between the active material and current collector) (see figure 1.13). Figure 2.8 presents the ideal Nyquist diagram that can be observed from three types of electrochemical cells (EDLC, pseudocapacitor, and battery). It is essential to present this diagram with 1:1 axis [21].

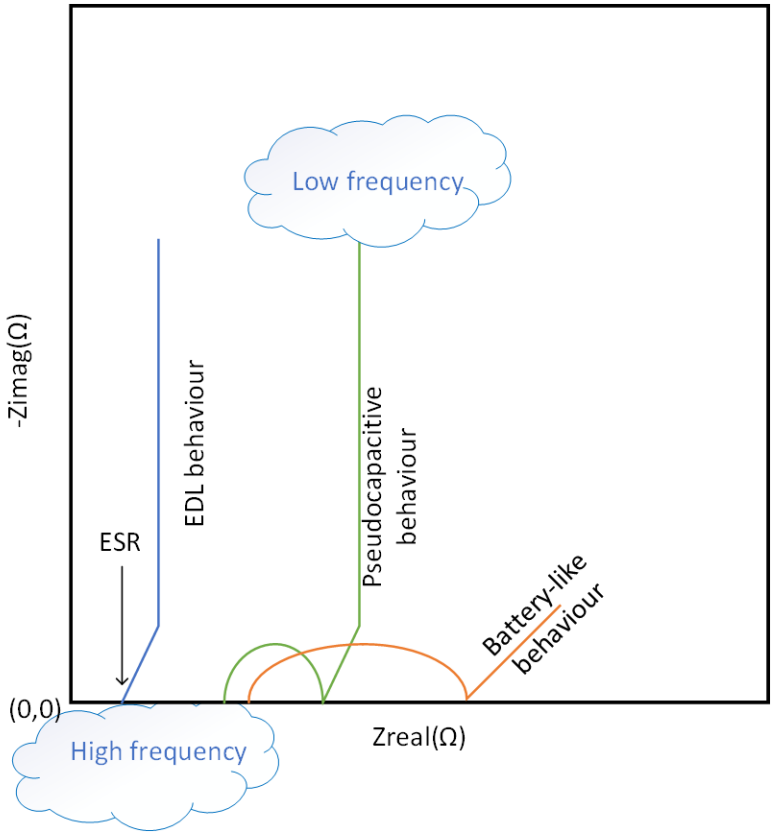

Figure 2.8: Ideal Nyquist plots in different types of EEC devices

The specific capacitance of electrochemical cells at the bias potential can be approximately calculated by equation 2.4 in the lowest value of frequency

range, from the nyquist diagram.

$$C[F/g] = \frac{1}{2\pi f.im\{Z\}} \frac{1}{m_{total}} \tag{2.4}$$

2.3.2 Cyclic voltammetry (CV)

CV is a technique performed with a potentiostat instrumental setup. A sweep potential, whose slope with respect to time determines the scan rate, is applied through the cell. The CV curve, which is the current of the cell versus the applied potential, is the output of this technique. According to the aforementioned descriptions in section 1.2, electrochemical cell charging mechanism, the specific capacity of EES, and potential window are some valuable information that can be evaluated from the CV technique [15].

2.3.3 Galvanostatic charge and discharge (GCD)

Despite the CV technique, GCD is based on the galvanostat setup in which a negative and positive constant current is applied so that the cell is charged and discharged. In order to find out the rate capability, the magnitude of the applied current is changed. The output data obtained in this technique can be observed through the potential profile during the charging and discharging periods of the cell with respect to time [21]. Rate performance and stability analysis in this work are performed based on the GCD technique.

2.3.4 Galvanostatic Intermittent Titration Technique (GITT)

The other possible useful technique based on the galvanostat is GITT. In an electrochemical cell, the diffusion is the net transfer of the active ions inside a solid electrode where the ions flow from the high concentration region to the lower one. According to the definition of the electrochemical diffusion, the **second Flick's law** is defined:

$$\frac{\partial C}{\partial t} = D \frac{\partial^2 C}{\partial x^2} \tag{2.5}$$

where x is the diffusion path into the solid electrode from the electrode/electrolyte interface, C is the local concentration, and D is the diffusion coefficient.
Considering the cell is composed of $A^{+z_A} + electrolyte$, and A_yB solid electrode, where y is the proportion of A species with respect to B. Performing the galvanostatic method, if the external current pulses (I) are applied over the cell, the value of y is changed. The variation of the composition ($\Delta\delta$ or Δy) in the solid electrode is evaluated according to the Faraday's law:

$$\Delta\delta = \frac{1}{z_A F n_B} \int_0^t I dt \tag{2.6}$$

where z_A is the charge number of the electroactive ions (A), F is the Faraday's constant, and n_B is the number of moles related to B species.
In order to solve the Eq. 2.5, the following initial and boundary conditions, according to the galvanostatic experiment, are considered:

$$C = C_0 \quad 0 \leq x \leq L, \quad t = 0 \tag{2.7}$$

$$-D\frac{\partial C}{\partial x} = \frac{I}{z_A F S} \quad x = 0, \quad t > 0 \tag{2.8}$$

$$\frac{\partial C}{\partial x} = 0 \quad x = L, \quad t \geq 0 \tag{2.9}$$

The initial concentration before applying the external current and in equilibrium condition is C_0. The Eq. 2.9 shows that the active ions (A) enter the solid electrode from the surface ($x = 0$). The boundary at the end of the path ($x = L$) is assumed as impermeable. In Eq. 2.8, S is the surface area of the electrode in contact with the electrolyte.
The result of the equation 2.5 is approximately shown in Eq. 2.10 for small time duration of current pulses ($\tau << L^2/D$).

$$C_s(t) - C_0 = \frac{2I\sqrt{t}}{z_A F S\sqrt{D\pi}} \tag{2.10}$$

where $C_S(t)$ is the surface concentration in time t. In the steady state, the charge transfer $\Delta\delta$ is shown as the following:

$$\Delta\delta = V_M(C_s - C_0) \tag{2.11}$$

here V_M is the molar volume of the electrode and C_s is the surface concentration in steady state. Eq. 2.12 is obtained, after differentiating Eq. 2.10 with respect to $\sqrt{t}$, multiplying it to dE (small variation of the potential) and considering Eq. 2.11.

$$\frac{dE}{d\sqrt{t}} = \frac{2IV_m}{z_A F S\sqrt{D\pi}}\frac{dE}{d\delta} \tag{2.12}$$

which can be written as:

$$D = \frac{4}{\pi}(\frac{IV_M}{z_A F S})^2(\frac{dE/d\delta}{dE/d\sqrt{t}})^2 \tag{2.13}$$

Since the duration of current pulses and the relaxation time are in the same order and intensity of the applied current is small, the expressions $\frac{dE}{d\sqrt{t}}$ and $\frac{dE}{d\delta}$ can be approximated $\frac{\Delta E_t}{\sqrt{\tau}}$ and $\frac{\Delta E_s}{\Delta\delta}$, respectively. ΔE_t is the potential variation during

the current pulse by not considering **iR drop** of the cell, happening immediately after the current application. ΔE_s is the steady state potential difference in two sequential relaxation.
As a result, the following approximated expression for diffusion is obtained:

$$D = \frac{4L^2}{\pi\tau}(\frac{\Delta E_s}{\Delta E_t}) \tag{2.14}$$

where L is the total diffusion path and equals to $V_M n_B/S$ [52, 53].

Chapter 3

Results and discussion

3.1 Physico-chemical characterization

3.1.1 XRD analysis

The XRD test is performed to analyze the crystallinity of the synthesized materials, including OMC, $OMC-WO_3-300$, $OMC-WO_3-400$, and $OMC-WO_3-600$. As figure 3.1 (a) shows, the amorphous properties of samples OMC, $OMC-WO_3-300$, and $OMC - WO_3 - 400$ are obvious since there is no crystalline peak in their XRD patterns. Considering the hybrid amorphous samples, there is a peak with low intensity at around $2\theta = 27^o$, which is matched with the previous work on amorphous WO_3 in [54] (figure 3.1 (b)). Interestingly, the crystalline structure of the sample $OMC - WO_3 - 600$ is obvious due to the sharp crystalline peaks. According to the literature, this XRD curve resembles orthorhombic WO_3 which is obtained at 700 ^oC in (PDF 00-020-1324 [55, 56] (figure 3.1 (c)).

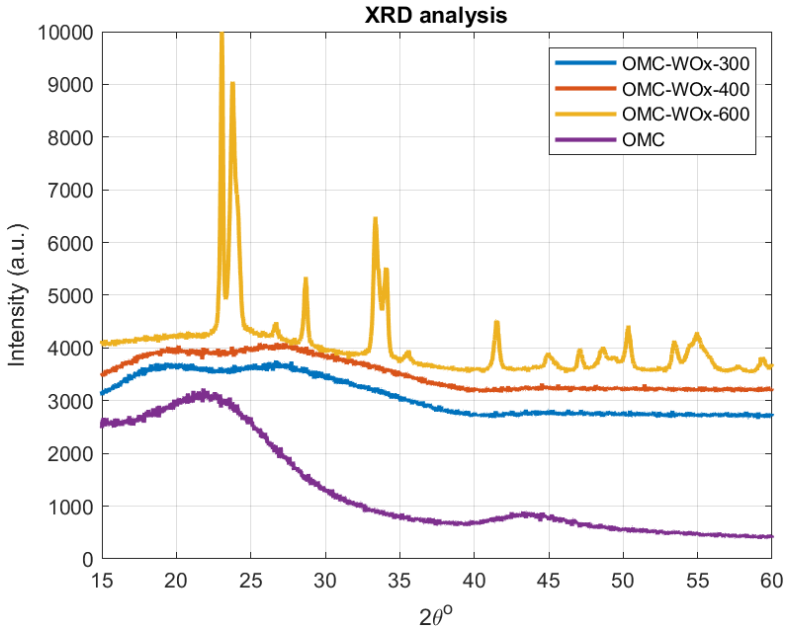

(a)

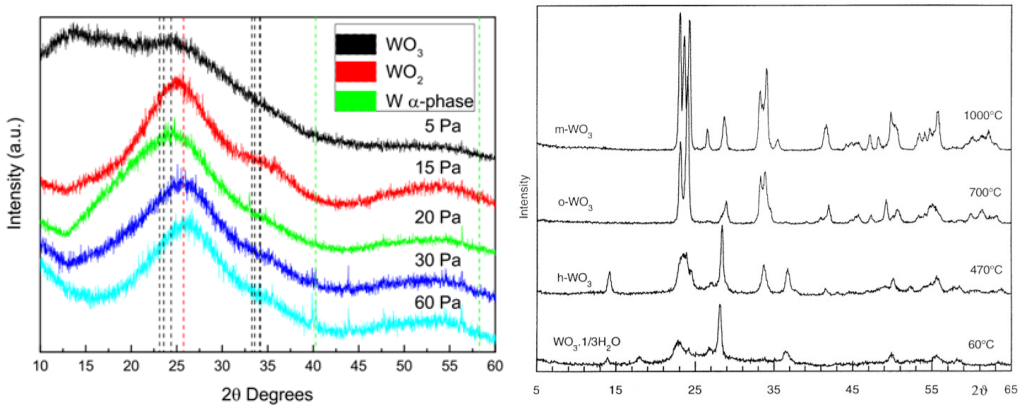

(b) (c)

Figure 3.1: (a) XRD results of the samples OMC, $OMC - WO_3 - 300$, $OMC - WO_3 - 400$, and $OMC - WO_3 - 600$ XRD, (b) XRD example of amorphous WO_3 [54] (c) XRD reference for orthorhombic WO_3 [55]

3.1.2 FESEM analysis

The FESEM technique is used to observe microscopic images in nano-scale samples as the following. The mesoporous carbon structure which is obtained form sucrose through the template SBA-15 (figure 3.2 (a)) is shown in figure 3.2 (b). Subsequently, figures 3.2 (c) and (d) illustrate $OMC - WO_3 - 300$ and $OMC - WO_3 - 400$.

Here, the WO_3 structures are not obvious, and the carbon mesoporous structure is relevant in the FESEM of both these samples.
Finally, the FESEM image of $OMC - WO_3 - 600$ can be another justification of the WO_3 crystalline structure in this hybrid material. The WO_3 particles are the evident adhered particles to the carbon textile (figures 3.3 (a) and (b)). These are the crystals, which are detected by XRD as well. Figures 3.3 (c) and (d) show orthorhombic WO_3 crystals in higher magnification; here, the OMC structure in the background portray can be distinguished from WO_3 particles.

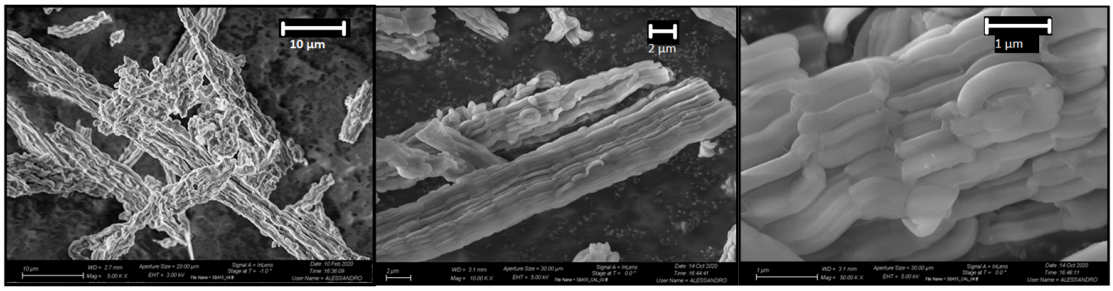

(a)

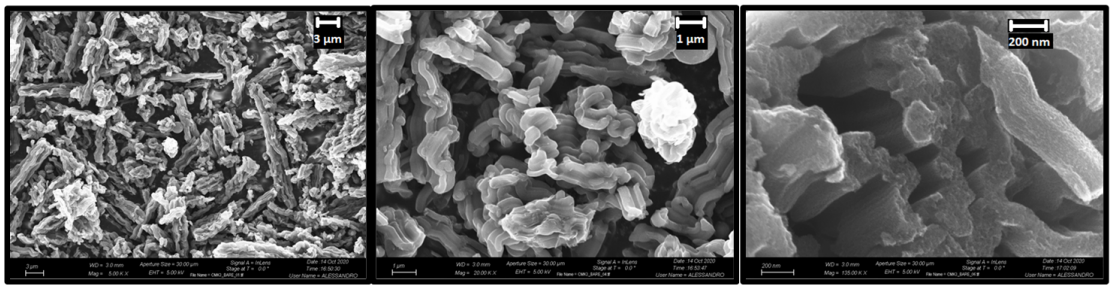

(b)

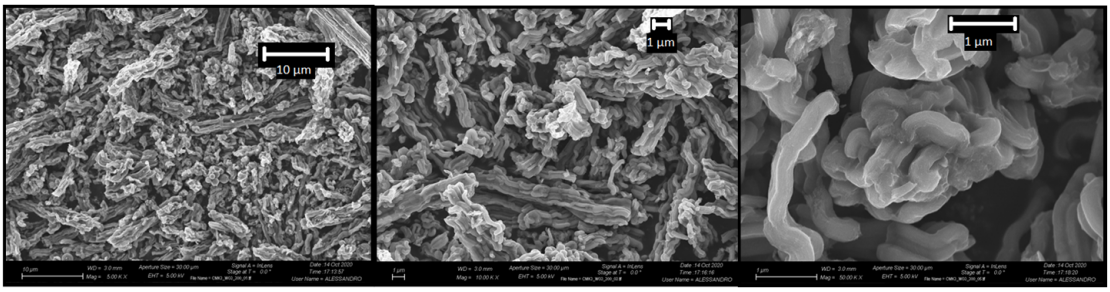

(c)

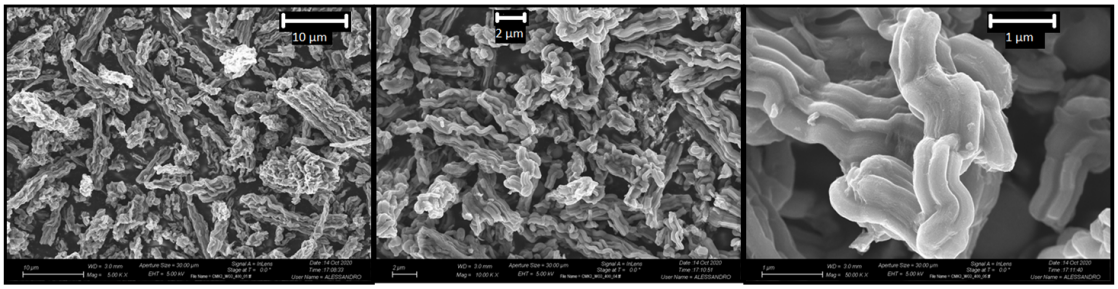

(d)

Figure 3.2: FESEM images (a) SBA-15, (b) OMC (c) $OMC - WO_3 - 300$, (d) $OMC - WO_3 - 400$

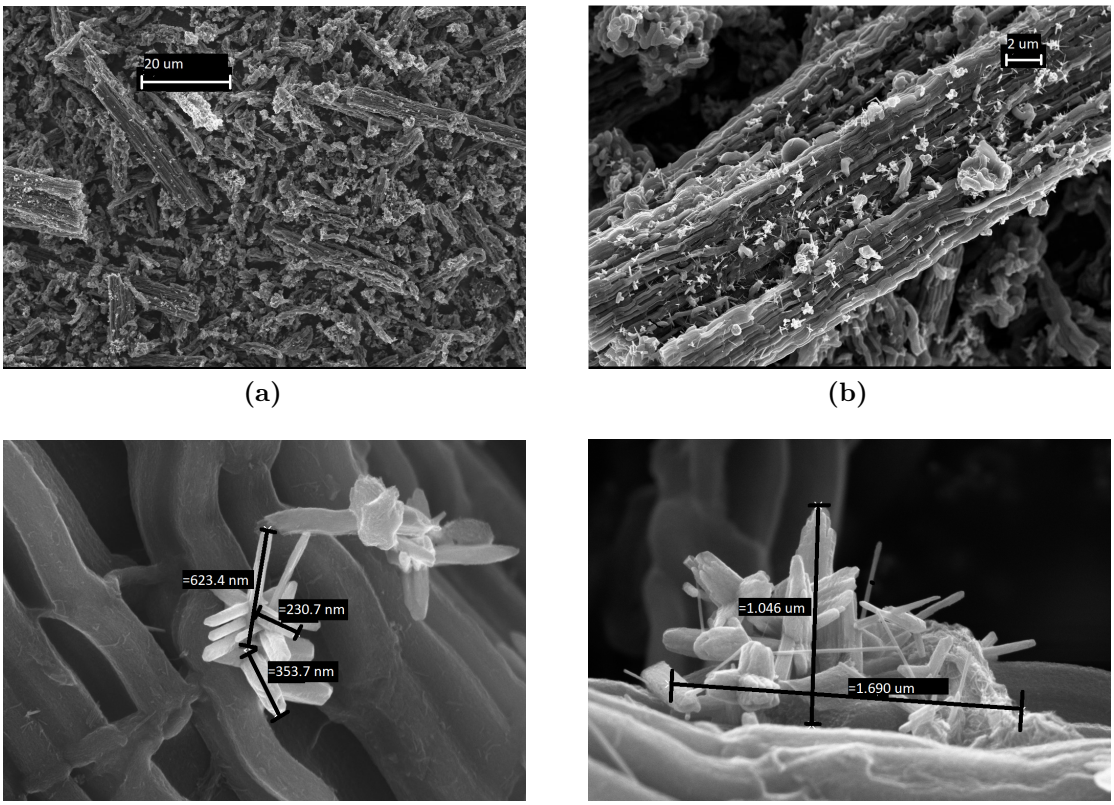

(a) **(b)**

(c) **(d)**

Figure 3.3: FESEM images of $OMC - WO_3 - 600$

3.1.3 Energy-Dispersive X-ray Spectroscopy (EDX)

As mentioned before, EDX is a method to analyze the composition of a sample and the proportion of each element. Figure 3.4 represent the EDX spectrum of OMC, $OMC - WO_3 - 300$, $OMC - WO_3 - 400$, and $OMC - WO_3 - 600$ in addition to their micrograph obtained by this method in which the spatial regions for performed EDX measurement have been specified. Firstly, the EDX spectra verify that the Si element has been almost completely washed out from the OMC sample after putting the composition at NaOH solution. The similar material properties of all three samples also can be verified, as they have identical X-ray spectra.

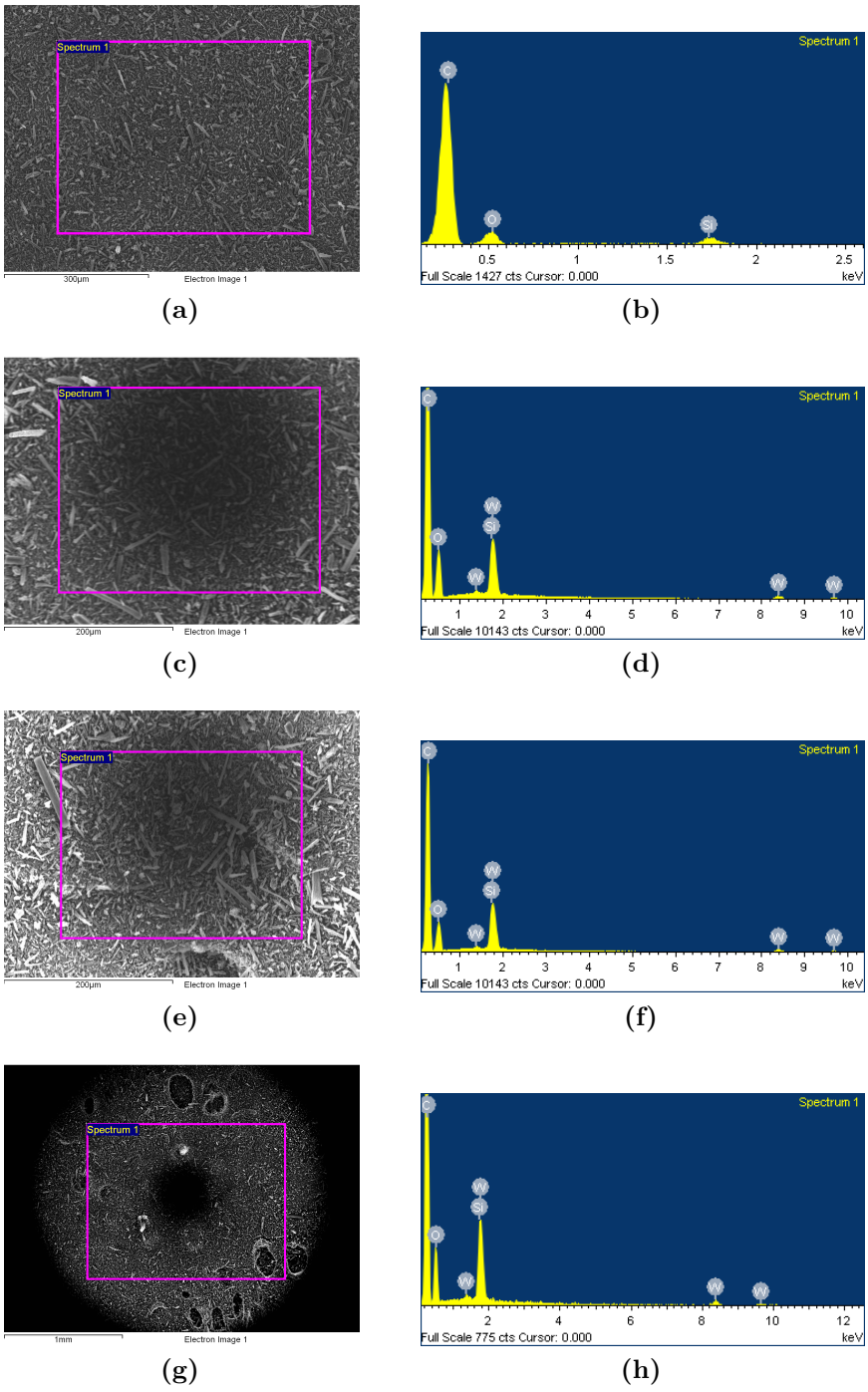

Figure 3.4: EDX micrograph and X-ray spectrum, respectively, of (a, b) OMC, (c, d) $OMC - WO_3 - 300$, (e, f) $OMC - WO_3 - 400$, (g, h) $OMC - WO_3 - 600$

As a consequence EDX measurements, the material atomic and weight composition ratio are provided in table 3.4. The low Si ratio shows the complete silica removal process from the obtained OMC. Considering the hybrid samples, despite the low atomic ratio of W, its weight ratio is almost 10% of the whole sample. As a result, the $OMC : WO_3$ proportion is approximately 87% : 13%.

Table 3.1: Weight and atomic ratio of elements in OMC, $OMC - WO_3 - 300$, $OMC - WO_3 - 400$, $OMC - WO_3 - 600$ from the EDX method

	OMC		$OMC - WO_3 - 300$		$OMC - WO_3 - 400$		$OMC - WO_3 - 600$	
Element	**Weight %**	**Atomic %**	**Weight %**	**Atomic %**	**Weight %**	**Atomic %**	**Weight %**	**Atomic %**
Carbon (C)	81.47	86.31	69.07	80.58	66.84	79.91	67.24	80.64
Oxygen (O)	15.46	12.29	20.35	17.82	19.89	17.85	19.09	17.19
Silicon (Si)	3.07	1.39	1.87	0.94	2.77	1.42	2.52	1.29
Tungsten (W)			8.71	0.66	10.50	0.82	11.15	0.87
Total	100							

3.2 Electrochemical characterization in water based electrolytes

3.2.1 Introduction

The data analysis and comparison of electrochemical characterization of three water-based cells, including OMC, $OMC - WO_3 - 300$, and $OMC - WO_3 - 400$, are presented in this section.
The first cell is based on the mesoporous structure, is likely to have a non-faradaic charge storage mechanism (or EDL). The other cells are based on hybrid material (WO_3 and OMC composition). Using the hybrid material as the electrode leads to hybrid energy storage mechanisms, including non-faradic energy storage, due to the OMC and faradic one thanks to the WO_3 layer. The reversible faradaic reaction (intercalation/deintercalation) of WO_3 particle with H^+ ions is presented in eq. 3.1 [57].

$$WO_3 + xH^+ + xe^- \rightleftharpoons H_xWO_3 \tag{3.1}$$

3.2.2 Coulombic efficiency and potential window

The CV analysis is first performed to find an optimum potential window for each cell. Incremental positive and negative potentials are applied to reach both the maximum and minimum sides of the potential window (PW), respectively. Here, the optimum potential window is defined as the coulombic efficiency of the cell is higher than 95%.
Regarding figure 3.5, OMC, $OMC - WO_3 - 300$, and $OMC - WO_3 - 400$ potential

windows are **[0.27 1.05] V, [-0.29 0.77] V, [-0.22 0.73] V** vs. Ag/AgCl, respectively.

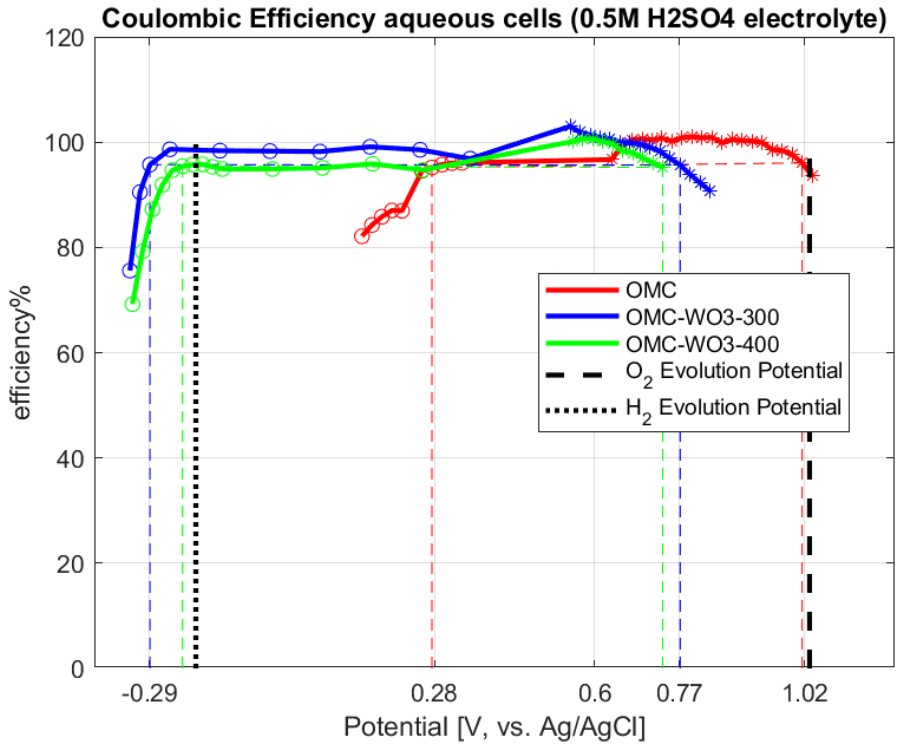

Figure 3.5: Coulombic efficiency, OMC, $OMC - WO_3 - 300^oC$, $OMC - WO_3 - 400^oC$ electrodes

Here, the oxygen (eq. 1.13) and hydrogen (eq. 1.14) evolution, which take action in the anodic and cathodic scans, respectively, at the interface between electrode and electrolyte solution, can be a reason of the decline in Coulombic efficiency [58].

3.2.3 CV analysis

Considering first the CV curves of $OMC - WO_3 - 300$ and $OMC - WO_3 - 400$ in variable scan rate, as shown in figure 3.6, the cathodic and anodic peaks on the lower side of potential windows are the reversible faradaic charge storage clues (equation 3.1) at the electrolyte-WO_3 interface. Due to the diffusion limits of the faradaic charge storage mechanism, the EDL charge storage is more relevant in higher scan rates, and the CV curve reaches a more rectangular shape. The charge storage contribution analysis of the water-based cells is presented in section 3.2.5. Table 3.2 presents the corresponding potential values vs. Ag/AgCl of anodic current

peaks in different scan rates. The small variation of these potentials by increasing the scan rate represents the pseudocapacitive characteristic (surface-controlled faradaic reaction) of the cells. That might be due to the amorphous material with high surface area ($OMC - WO_3$) in which ion diffusion is not playing roles in the charging/discharging process, unlike conventional batteries [2]. The other important fact, which is evident in table 3.2 and fig. 3.6, is the decrease of the current density on the left side of the potential window as the scan rate increases.

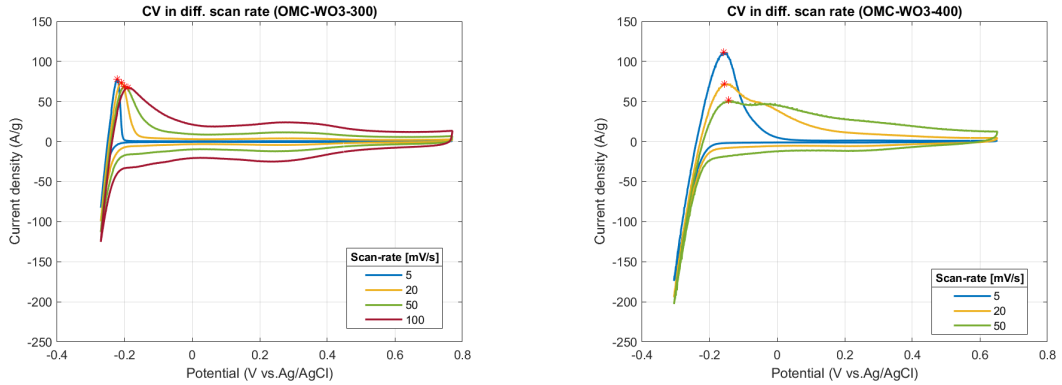

(a) **(b)**

Figure 3.6: CV analysis in different scan-rates, electrode active materials: (a) $OMC - WO_3 - 300$, (b) $OMC - WO_3 - 400$

Table 3.2: The **anodic current peaks** due to the deintercalation reaction in full window CV curve and different scan-rates

	$OMC - WO_3 - 300^oC$		$OMC - WO_3 - 400^oC$	
Scan-rate [mV/s]	**Potential [V]**	**Specific current [A/g]**	**Potential [V]**	**Specific current [A/g]**
5	-0.2221	77.7377	-0.1585	111.28
6	-0.2208	76.8386	-0.1574	105.87
8	-0.2178	76.3718	-0.1565	100.09
10	-0.2155	75.5937	-0.154	93.11
20	-0.2102	73.7263	-0.1502	71.67
40	-0.2029	69.9916	-0.1436	55.92
50	-0.2007	68.7467	-0.1404	51.63
60	-0.1985	67.7438	-0.1361	49.54
80	-0.1921	67.0349	-0.1234	46.22

The CV curves of the three cells are analyzed together in order to examine the possibility of assembling a complete device with positive (OMC) and negative ($OMC - WO_3$) electrodes (Fig.3.7). On the left side of the window in the CV curves of $OMC - WO_3 - 300$ and $OMC - WO_3 - 400$, a reversible oxidation peak

is observed in the anodic sweep, while its corresponding reduction peak is not recognizable in the cathodic sweep, probably, owing to the higher decline of the current density during the hydrogen evolution. In addition, two broad anodic and cathodic faradaic peaks with low current density can be seen in the CV curve of OMC around 0.3 V, which can be due to quinone-like groups' redox reaction in contact with the aqueous electrolyte [40].

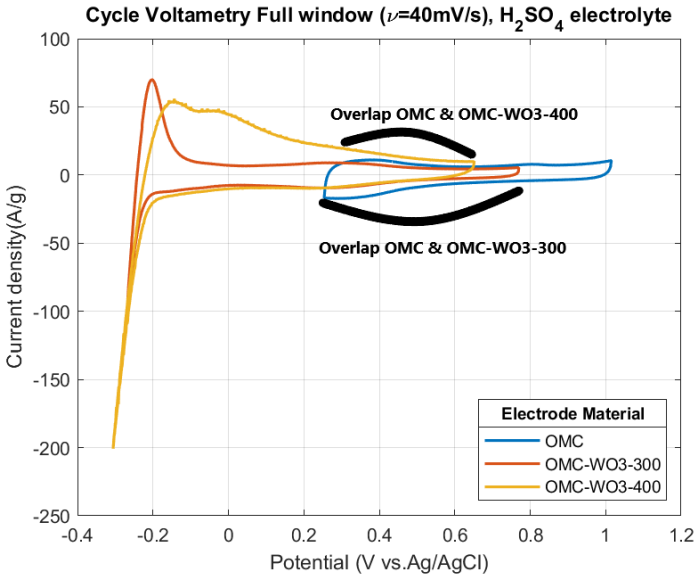

Figure 3.7: CV curve and Specific current , OMC, $OMC - WO_3 - 300$, $OMC - WO_3 - 400$ electrodes with scan rate= 40 mV/s

3.2.4 Charge density and the rate capability

WO_3 is likely to be based on faradaic charge storage mechanism [58], while it is expected to reach EDLC from OMC active layer; as a result, the specific capacity can be the proper choice to analyze both rate and energy storage capability of the cells [21].
Figure 3.8 shows the specific capacity obtained from $OMC - WO_3 - 300$, $OMC - WO_3 - 400$, and OMC cells. The higher charge density of $OMC - WO_3 - 400$ than $OMC - WO_3 - 300$ in lower scan rates can be due to the broader anodic peak. This figure also depicts the extremely high capability of WO_3 particles to store a much higher charge compared to OMC due to the intercalation reaction of WO_3 at the surface (eq.3.1). The maximum OMC charge storage is observed at the scan rate of 40 mV/s; thus, this scan rate can be considered an optimum value for designing an asymmetric EES device. The following table compares the total charge densities for each cell when $\nu = 5$ and 40 mVs^{-1}.

Table 3.3: Specific capacity of the cells in $\nu = 5$ and $\nu = 20\ mVs^{-1}$

	Specific capacity [mAh/g]	
Material	v=5 $[mVs^{-1}]$	v=40 $[mVs^{-1}]$
OMC	37.4	40.8
$OMC - WO_3 - 300$	141.27	75.5
$OMC - WO_3 - 400$	732.2	162.1

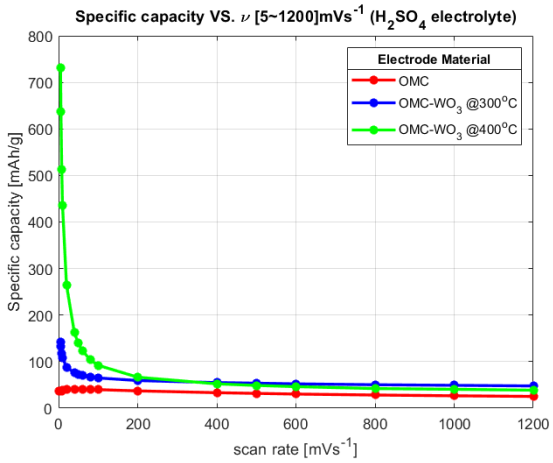

Figure 3.8: Specific capacity vs. scan rate (Rate capability analysis) of aqueous cells

3.2.5 Charge storage contribution analysis

Trasatti method

According to equation 3.2, the stored charge at the electrode can be splitted into the surface (Q_s) and diffusion (Q_d) controlled charges.

$$Q = Q_s + Q_d \tag{3.2}$$

where the surface charge itself includes **inner** (less accessible) and **outer** (more accessible) charge contributions:

$$Q_s = Q_{s,in} + Q_{s,out} \tag{3.3}$$

According to an assumption, the following boundary conditions are defined, with the aim of surface-controlled charge evaluation:

$$Q_s = \begin{cases} Q_{s,out}, & \text{if } \nu = \infty \\ Q_{s,in} + Q_{s,out}, & \text{if } \nu = 0 \end{cases} \tag{3.4}$$

Considering a linear relationship between Q_d and $\nu^{-1/2}$, eq. 3.2 can be rewritten as following:

$$Q = Q_{s,out} + A_1\nu^{-1/2} \tag{3.5}$$

here A_1 is a constant and the outer surface-controlled charge is obtainable at a very high scan rate. The inverse of the total charge also can be shown as in eq. 3.6, which leads to evaluate the total Q_s from y-axis intercept of this linear equation. A_2 is a constant in this equation.

$$Q^{-1} = Q_s^{-1} + A_2\nu^{1/2} \tag{3.6}$$

The ohmic loss and irreversible chemical reactions are not considered in this method, and the charge evaluation is reliable only in a certain interval of scan rate [13].

Discussion on charge storage contribution of water-based cells

According to figure 3.9 (a), the total surface charge of $OMC - WO_3 - 400$ is the highest; however, the lowest outer surface-controlled charge (the charge value in the highest ν) of this cell (figure 3.9 (b)), compared to the other cells, can indicate the low level of non-faradaic contribution. Thus, even though the general surface-controlled charge storage of OMC is the lowest, considering the higher scan rates, interestingly, the outer charge, which is mainly attributed to the non-faradaic mechanism, is relevant in this cell.

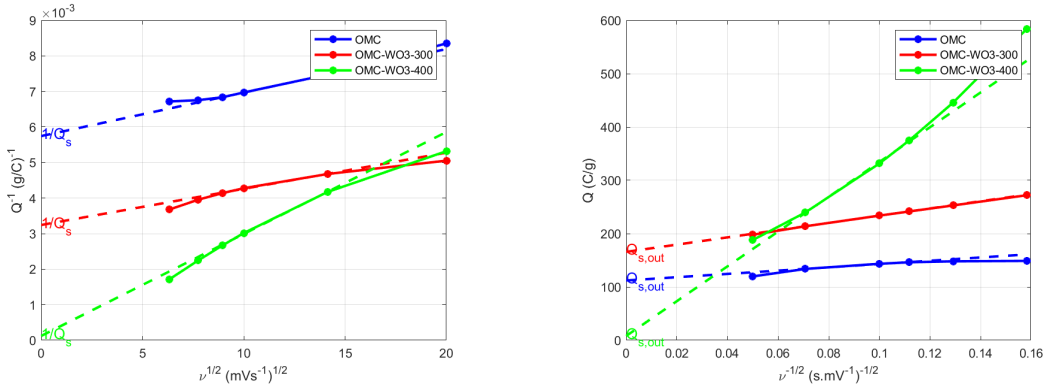

(a) **(b)**

Figure 3.9: (a) The surface-controlled and (b) outer surface-controlled charge analysis of water-based cells

3.2.6 Electrochemical Impedance Techniques & Stability

The cells' life cycle is analyzed by monitoring the stability of capacitance and uncompensated resistance through the EIS test after performing the GCD measurements within the previously measured potential window. According to figure 3.10, both capacitance and series resistance of the cells with $OMC - WO_3$ electrode remain stable after 5000. Besides, the equivalent series resistance of OMC cell remains stable while the capacitance even increases after 15000 cycles. Considering the equivalent electrical circuits (figure 1.13), the resistance and capacitance are measured by applying the aforementioned methods in section 2.3.1. Here in figure 3.10 (a), the higher capacitance of OMC is due to the biasing point, which is 0 with respect to the open circuit potential of each cell; in other words, the general capacitance of the hybrid material is higher if the whole potential window is evaluated. The Nyquist diagram of the cells is depicted in figure 3.10 (c), after 5000 cycles. As all cells are operating at the OCP, the surface-controlled charging mechanism is relevant; as a result, according to figure 2.8, the semicircle does not appear in their Nyquist plot.

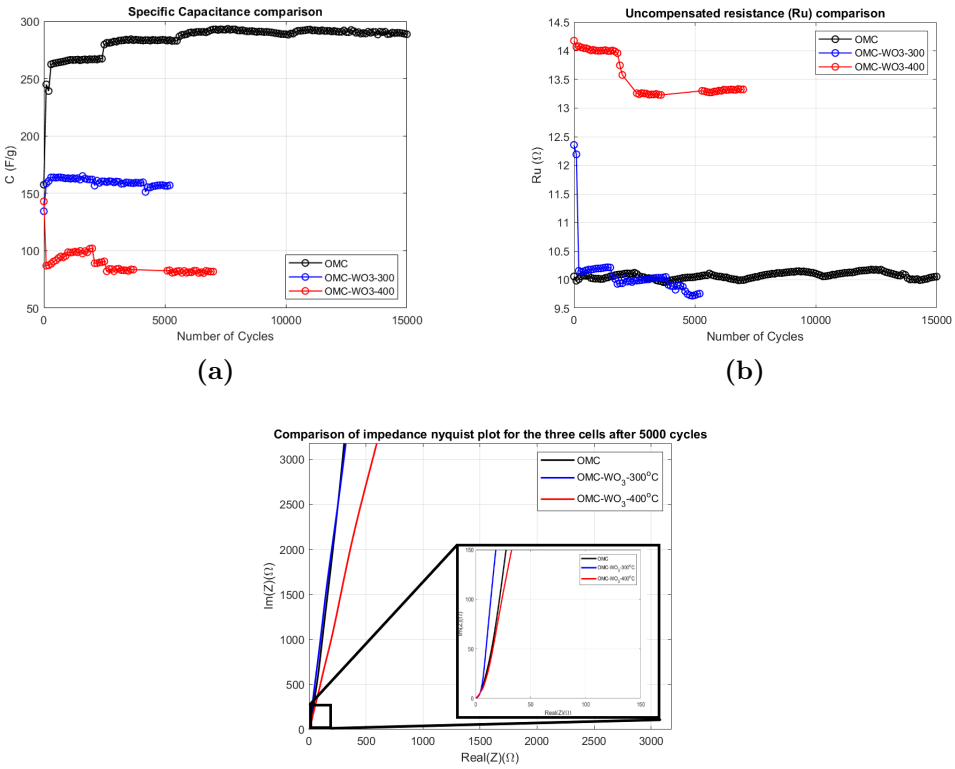

Figure 3.10: EIS analysis of OMC, $OMC - WO_3 - 300$, $OMC - WO_3 - 400$ samples (a) Uncompensated resistance (Ru) vs. number of cycles, ohm, (b) Specific capacitance vs. number of cycles, F/g (c) Nyquist plot at 500th cycle

3.2.7 Literature review conclusion

The table 3.4 provides a detailed comparison of the electrochemical properties of selected WO_3-based cells with aqueous solution electrolyte in previous works.

Table 3.4: Comparison of electrochemical properties of selected WO_3-based cells with water-based electrolyte

Material	Electrolyte	Charge density (Cg^{-1})	Rate	Potential Window (V vs. RE)	Capacity retention %	ref
Hexagonal WO_3	1 M H_2SO_4	408	2 mVs^{-1}	(-0.5, 0.45)	87%, 5000 cycles	[59]
WO_3 cubic	0.5M H_2SO_4	304	1 Ag^{-1}	(-0.4, 0.2)	97%, 5000 cycles	[60]
Ordered Mesoporous Tungsten Oxide	2 M H_2SO_4	67	0.5 mVs^{-1}	(-0.1, 0.8)	NA	[61]
WO_3 nanoplates	1 M H_2SO_4	363.6	2 Ag^{-1}	(-0.6, 0)	89%, 5000 cycles	[62]
Hexagonal crystal WO_3/Carbon Cloth	0.5 M H_2SO_4	333.6	0.5 mVs^{-1}	(-0.5, 0.3)	99.3 %, 5000 cycles	[63]
WO_3	H_2SO_4 + Hydroquinone	355	5 mVs^{-1}	(-0.5, 0)	97%, 3000 cycles	[25]
$OMC - WO_3 - 300$	0.5M H_2SO_4	508.6	5 mVs^{-1}	(-0.27, 1.05)	96%, 5000 cycles	this work
$OMC - WO_3 - 400$	0.5M H_2SO_4	2636	5 mVs^{-1}	(-0.22, 0.73)	80%, 5000 cycles	this work

In summary, WO_3 composite electrode can provide a high potential window on the negative side with respect to the reference, in addition to the high capacity due to the diffusion control mechanism, which brings us to anticipate a complete EES device including $OMC - WO_3$ and OMC as the anode and cathode, respectively. However, the usage of water solution as an electrolyte comes with several limitations. The potential windows of WO_3 and OMC electrodes are limited due to the H_2 and O_2 evolution, respectively. According to figure 3.6, decremental current density was observed in higher scan rates of WO_3 electrode, which might be due to the H_2 evolution in the lower side of potential. Likewise, the electrolyte leakage can be counted as another drawback of such cells. Consequently, these circumstances bring us to perform the same analysis for an aprotic coin cell which can resemble the commercial anticipation more than aqueous cells.

3.3 Electrochemical characterization in organic solvant electrolyte

3.3.1 Cell specification

The electrochemical properties of the Li-ion based coin cells including OMC, $OMC - WO_3 - 300$, $OMC - WO_3 - 400$, and $OMC - WO_3 - 600$ are presented in this section.

3.3.2 CV technique & Solid electrolyte interphase (SEI) layer creation

The initial Open Circuit Potential (OCP) of $OMC-WO_3-300$, $OMC-WO_3-400$, and $OMC - WO_3 - 600$, before the cells' stability, are measured as 3.086, 2.854, and 3.175 V, respectively. The cyclic voltammetry experiments are performed within potential window $= [0.2 - OCP]V$ vs. Li/Li^+. Figure 3.11 shows the first cycle of CV curves. The appearance of large cathodic peaks around 0.6 V vs. $Li/Li+$ in the first CV cycle of all the cells can be associated with the Li-ion electrolyte decomposition on the solid anode and generation of SEI layer in the first cathodic cycle as the reverse anodic peak cannot be observed [27]. Besides, what is notable in $OMC-WO_3-600$ is another irreversible reaction (SEI creation) around 2.5 V, which can prove the crystalline structure in this sample [64].

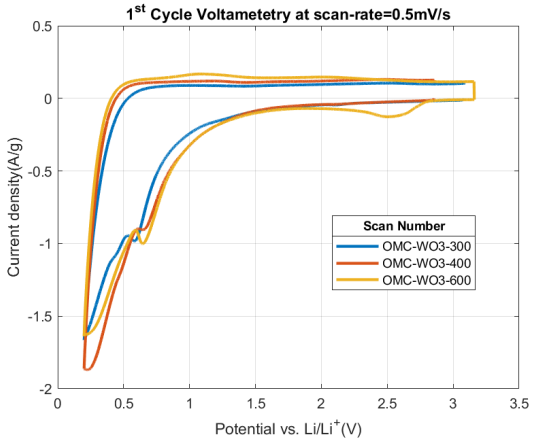

(a)

Figure 3.11: The first CV cycle of the hybrid aprotic coin cells $OMC-WO_3-300$, $OMC - WO_3 - 400$, and $OMC - WO_3 - 600$,

Figure 3.12 presents five subsequent CV cycles of the samples. There is still

evidence of the irreversible chemical reactions in the second and third cycles. However, after the fourth cycle, the CV curves have a stable shape with reversible intercalation reactions with similar energy states (potential peaks) in each cycle.

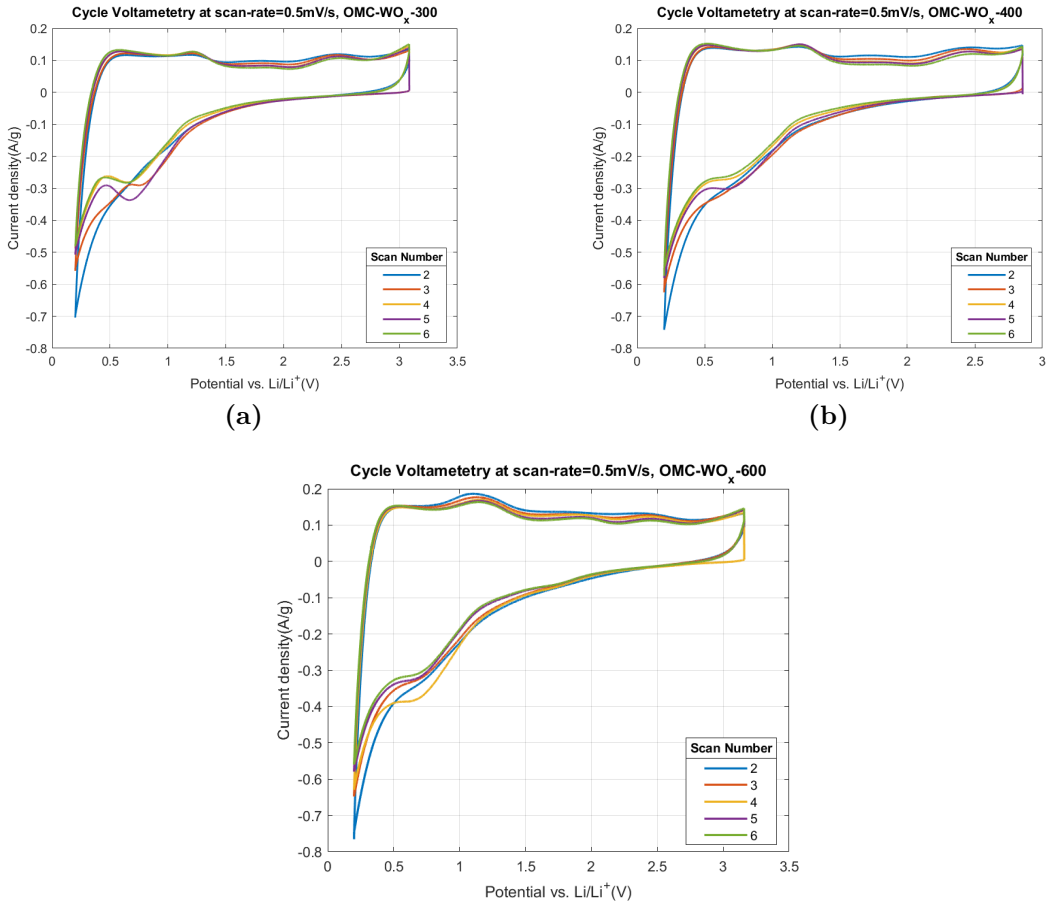

Figure 3.12: CV curve from the 2nd to 6th cycle of the new coin cells (a) $OMC - WO_3 - 300$, (b) $OMC - WO_3 - 400$, and (c) $OMC - WO_3 - 600$

The peaks appearing in the cathodic and anodic sweeps in the higher CV cycles can be associated with the intercalation (eq.3.7) and deintercalation reactions (eq, 3.8) of Li-ions, respectively [27, 65].

$$WO_3 + xLi^+ + xe^- \rightarrow Li_xWO_3 \tag{3.7}$$

$$Li_xWO_3 \rightarrow WO_3 + xLi^+ + xe^- \tag{3.8}$$

Figure 3.13 also shows a comparison diagram of CV experiment of all $OMC - WO_3$ electrodes when the scan rate is 0.5 mV/s. The specified potential window of each cell provides stable cells with Coulombic efficiency higher than 95%. The CV curves in this figure are obtained after 20 cycles when the initial stability of the cells and SEI layer creation are fulfilled. In this figure, the consistent oxidation peak of all three samples around 1.2 V can associate with the corresponding reduction shoulder at 0.9 and 0.75 V for amorphous and crystalline samples, respectively [27, 64, 65, 66]. Another cathodic shoulder and its relative anodic peak appear in the CV of $OMC - WO_3 - 600$, around 1.7 and 2 V, respectively, which were also observed in the previous works [27, 65].

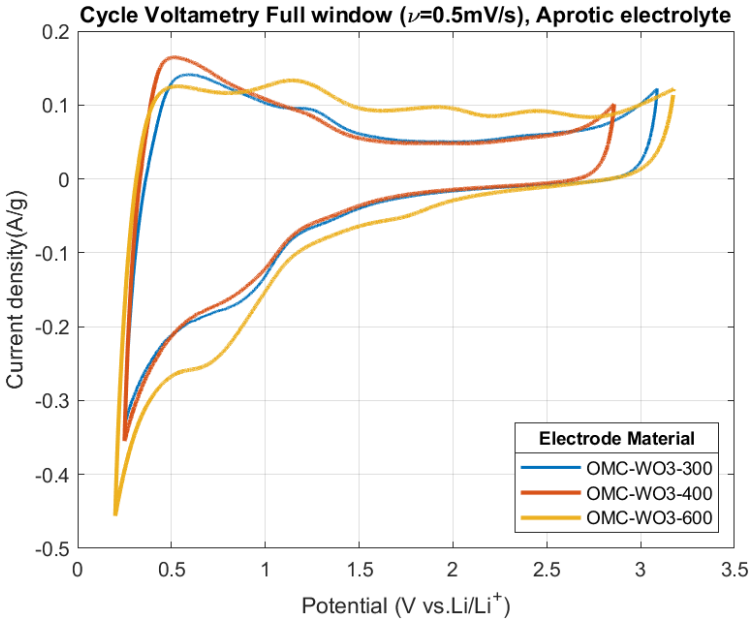

Figure 3.13: CV curve of $OMC - WO_3 - 300$, $OMC - WO_3 - 400$, and $OMC - WO_3 - 600$

3.3.3 Coulombic efficiency and potential window

Regarding eq.1.12, the potential windows of the coin cells OMC, $OMC - WO_3 - 300^oC$, 400^oC, and 600^oC are determined by targeting the coulombic efficiency higher than 95%. According to figure 3.14 (a), the potential window of OMC cell is [2.9–4] V vs. Li/Li^+.
Concerning $OMC - WO_3 - 300$, $OMC - WO_3 - 400$, and $OMC - WO_3 - 600$, the maximum value of the applied potential is set at the initial OCP of each cell (mentioned before), and the minimum side of the potential window is variable in order to evaluate the Coulombic efficiency in different potential windows.

Consequently, the selected minimum side of the potential window of amorphous cells is 0.25 V, and the crystalline one is 0.2 V vs. Li/Li^+, so that the Coulombic efficiency higher than 95% can be reached (figure 3.14 (b)).

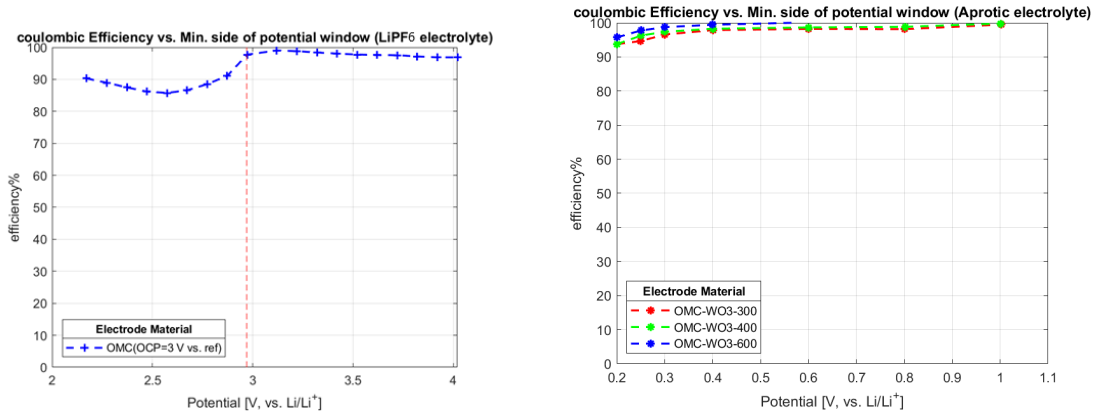

(a) **(b)**

Figure 3.14: Coulombic efficiency of the aprotic coin cells (a) OMC, (b) $OMC-WO_3-300$ & $OMC-WO_3-400$ & $OMC-WO_3-600$

3.3.4 Specific capacity and the rate capability of the cells

The specific capacity of each coin cell versus the scan rate in the aforementioned potential windows is illustrated in figure 3.15. Additionally, table 3.5 presents the charge densities of cells when the scan rate is 0.5 and 4 mVs^{-1}. The scan rate analysis is performed after stabilization of the electrodes.

Table 3.5: Specific capacity of the coin cells with Li-ion cell electrolyte

	Specific capacity [mAh/g]	
Material	v=0.5 $[mVs^{-1}]$	v=4 $[mVs^{-1}]$
OMC	4.64	13.05
$OMC-WO_3-300$	124.1	79.6
$OMC-WO_3-400$	116.7	84
$OMC-WO_3-600$	209.17	100

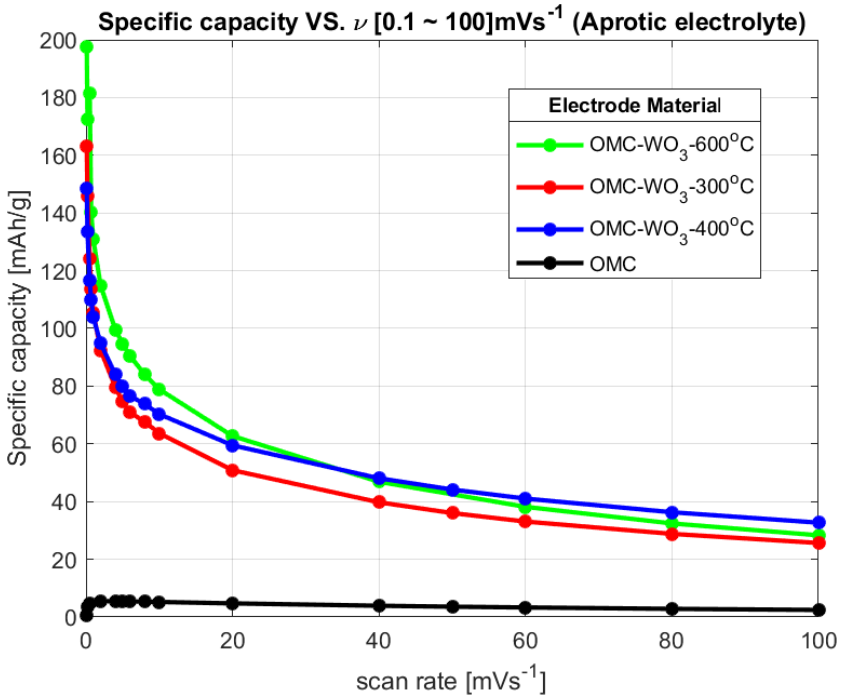

Figure 3.15: Charge density vs. scan rate, aprotic coin cells, OMC, $OMC - WO_3 - 300$, $OMC - WO_3 - 400$, and $OMC - WO_3 - 600$

According to figure 3.15, even though the OMC capacity is almost constant with respect to scan rate, the maximum specific capacity in this sample is observed at $\nu = 4mVs^{-1}$. As a result, illustrating the CV curve of all samples in a single figure (figure 3.16) at this optimum scan rate would be profitable in order to analyze the possibility of asymmetric energy storage device fabrication, including the hybrid material ($OMC - WO_3$) as the negative electrode and OMC as the positive one. Consequently, the maximum expected potential window of this anticipated device would be around 3.8 V by considering $OMC - WO_3 - 600$ as the negative electrode. It can be notable that the amorphous samples' faradaic peaks disappear as soon as the scan rate increases, while these peaks are not negligible at this scan rate in the crystalline sample. This can show the higher impact of the diffusion-controlled mechanism in the latter sample.

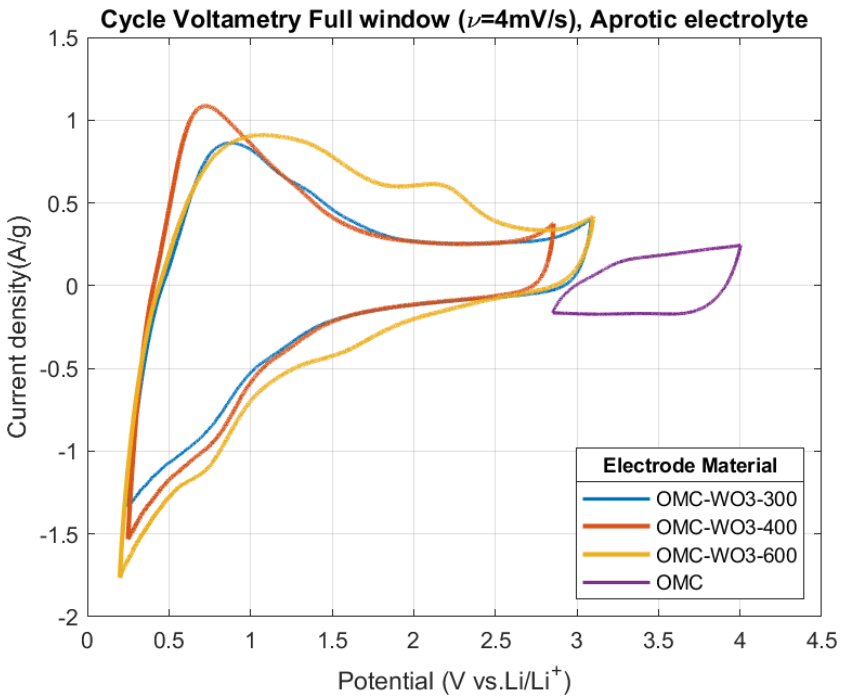

Figure 3.16: CV curves of half cells: OMC, $OMC-WO_3-300$, $OMC-WO_3-400$, and $OMC-WO_3-600$ at $\nu = 4mVs^{-1}$

3.3.5 Charge storage contribution analysis

Lindstrom et al. method The specific current of each energy storage contains a diffusion-controlled and a surface-controlled contribution. In general, the relation between the current and the scan rate is defined as:

$$i = a\nu^b \tag{3.9}$$

This equation can be presented in a linear form in the logarithmic scale:

$$log(i) = log(a) + blog(\nu) \tag{3.10}$$

here b alternates from 0.5 to 1, depending on charging mechanism. When b=*1*, the process is surface-controlled where the stored energy can be either due to the EDL (eq.3.11) or surface-confined redox (eq. 3.12).

$$i = C_{DL}\nu \tag{3.11}$$

where C_{DL} is the double layer capacitance.

$$i = \frac{nF^2}{4RT}\Gamma^*\nu \tag{3.12}$$

n is the number of transferred electrons and Γ^* is the amount of redox active adsorbed species at the surface (mol). The diagnosis of EDL from surface-confined redox is not possible in this method. If *b=0.5*, the reaction is diffusion-controlled, which presented with Randles-Sevcik equation:

$$i = 0.4958nFAC^*.D^{1/2}(\frac{\alpha nF}{RT})^{1/2} \tag{3.13}$$

where C^* is the concentration of the reduced ions in the electrode and α is the transfer coefficient. The eq. 3.13 is proposed to evaluate the diffusion coefficient, valid only in the semi-infinite diffusion control where the diffusion length is much larger than $\sqrt{Dt_d}$ (t_d is the diffusion time). Locating b between 0.5 and 1 can be the result of either mixed control or finite diffusion length [13, 67].

Discussion on charge storage contribution of aprotic cells

By implementing the current contribution method, the corresponding current contribution of hybrid samples is shown in figure 3.17. Subsequently, the modification capability of the cells to monitor the energy storage mechanism (surface-controlled or diffusion-controlled), depending on the charging/discharging rate, can be an interesting feature to find out the scan rate providing optimum power and capacity, which can be analyzed through this method.

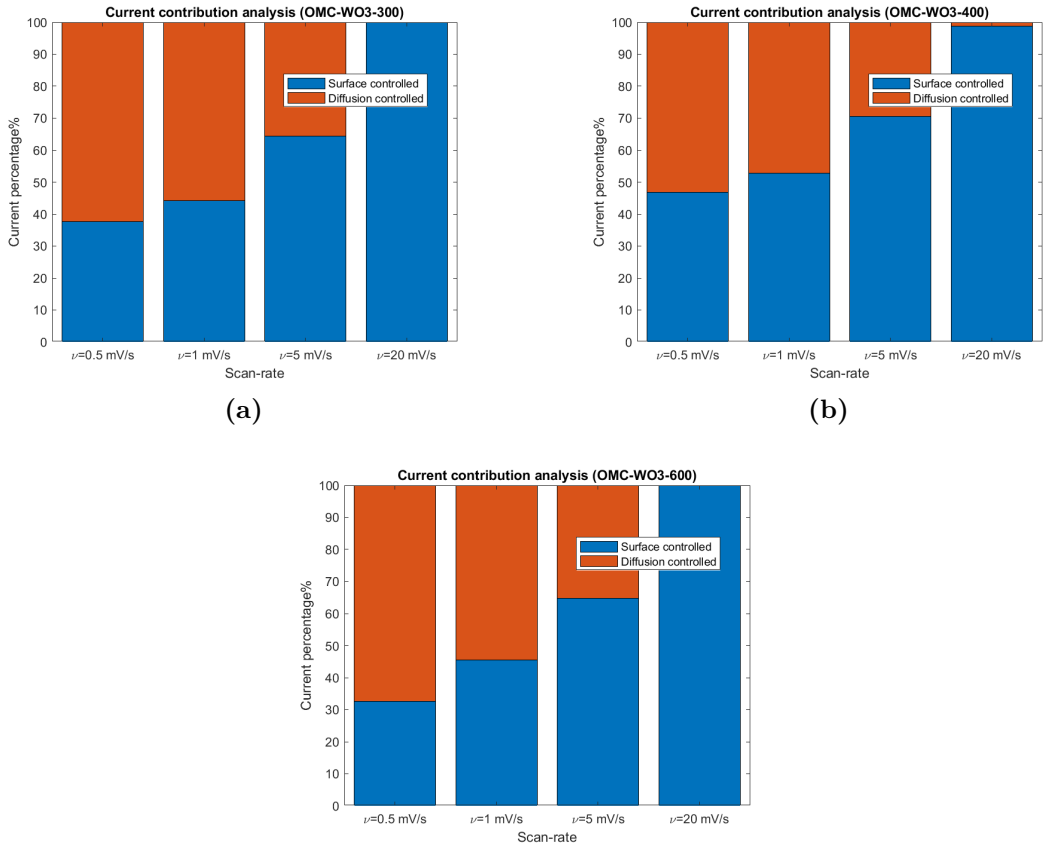

Figure 3.17: Energy storage mechanism analysis based on the current contribution (a) $OMC - WO_3 - 300$, (a) $OMC - WO_3 - 400$, and (c) $OMC - WO_3 - 600$

3.3.6 Diffusion coefficient evaluation (GITT)

As observed in the previous section, the diffusion-controlled mechanism plays an essential role in the charging/discharging process at lower rates. Consequently, the diffusion coefficient evaluation of Li-ions can be profitable so that the mass transfer of ions into/from the electrode material can be analyzed. This can be reached using GITT as an approximation technique for diffusion coefficient calculation (section 2.3.4).

The C-rate is defined as the applied current at the GCD technique in which the whole charging or discharging process of energy storage takes 1 hour. Subsequently, the diffusion coefficient of the samples $OMC - WO_3 - 300$ and $OMC - WO_3 - 400$ are measured when the charging/discharging rate is 0.1C so that the applied current density is measured as 17.9 and 16.8 mA/g, respectively.

Figures 3.18 (a) and (b) depict a complete charging and discharging process of GITT curves of both samples. Here, the applied current pulse period (τ) is 15 min with a 50% duty cycle. Two subsequent charging steps and discharging steps are illustrated in figure 3.18 (c) and (d).

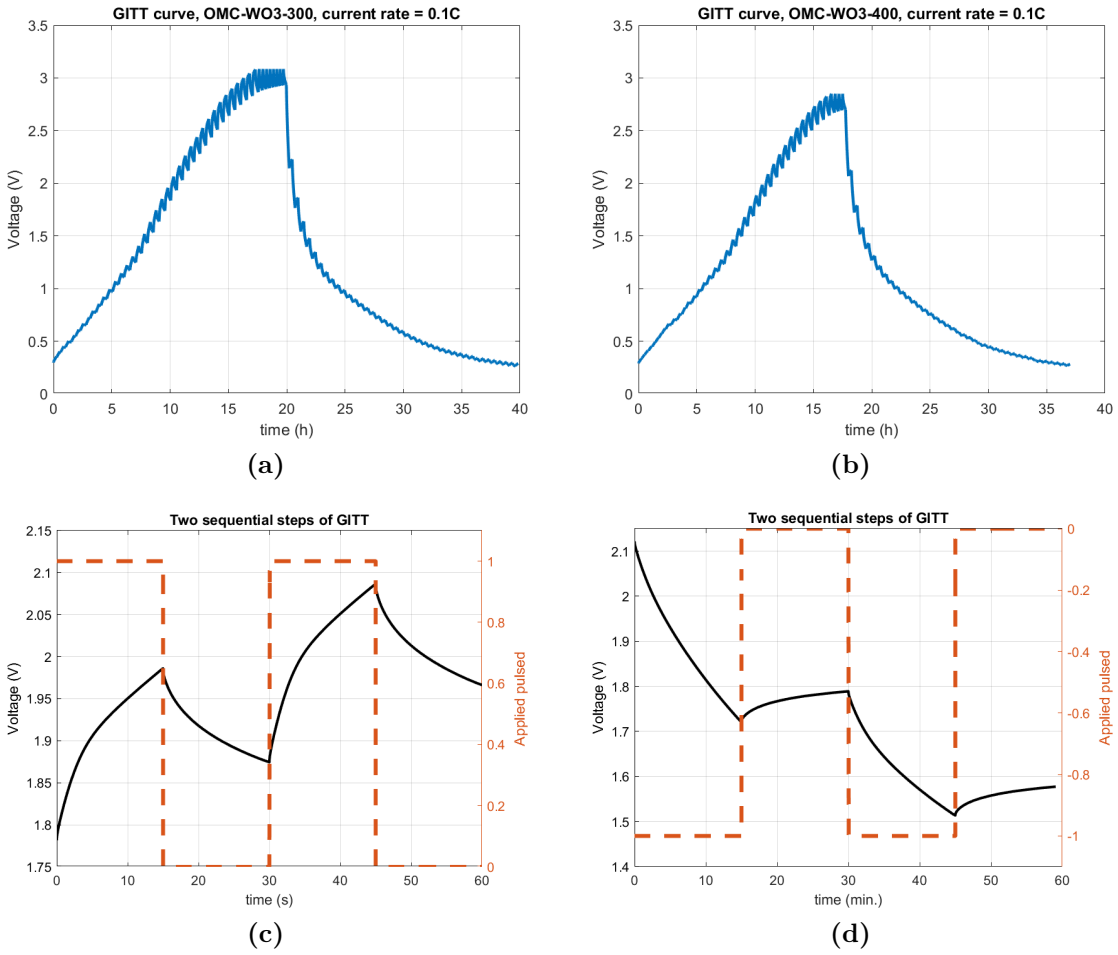

Figure 3.18: (a,b) The GITT curves of samples $OMC - WO_3 - 300$ and $OMC - WO_3 - 400$, respectively; (c,d) two sequential charging and discharging steps of GITT curve, respectively, with corresponding applied current pulse

The diffusion coefficient is evaluated according to equation 2.14. According to the mentioned coin cell characterizations, the electrode surface is 1.77 cm^2; consequently, the thickness of WO_3, the active layer where the redox reaction takes place, can be approximately evaluated by knowing the total volume of this material ($L = V_{WO_3}/S$). Here, the active electrode mass of $OMC - WO_3 - 300$

and $OMC - WO_3 - 400$ are measured 3.3 and 2.85 mg, respectively. Since 30% of these electrodes are composed of WO_3, the corresponding WO_3 mass can be measured. Assuming the ideal fraction of O/W = 3, since it has been shown that both samples are amorphous, regarding figure 3.19 obtained from [54], the mass density of WO_3 would be 4.8 g/cm^3. Accordingly, the diffusion coefficients of both samples in each GITT step (both charging and discharging stages) are calculated. As shown in figure 3.20, the diffusion coefficient of $OMC - WO_3 - 300$ is generally higher. This difference is significant in the lower voltages in the charging phase, which can justify a higher diffusion-controlled current of $OMC - WO_3 - 300$.

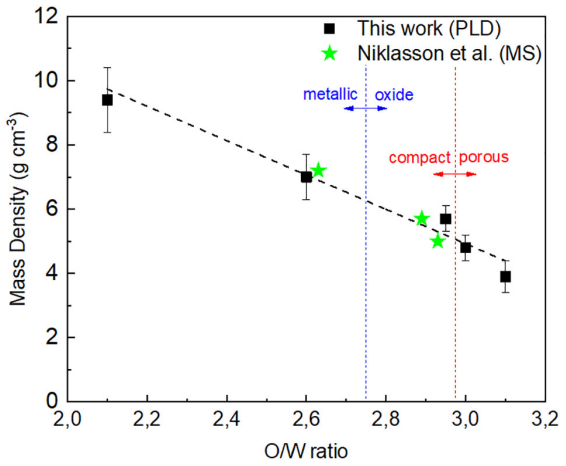

Figure 3.19: Mass density of WO_3 versus the W/O ratio (obtained from [54])

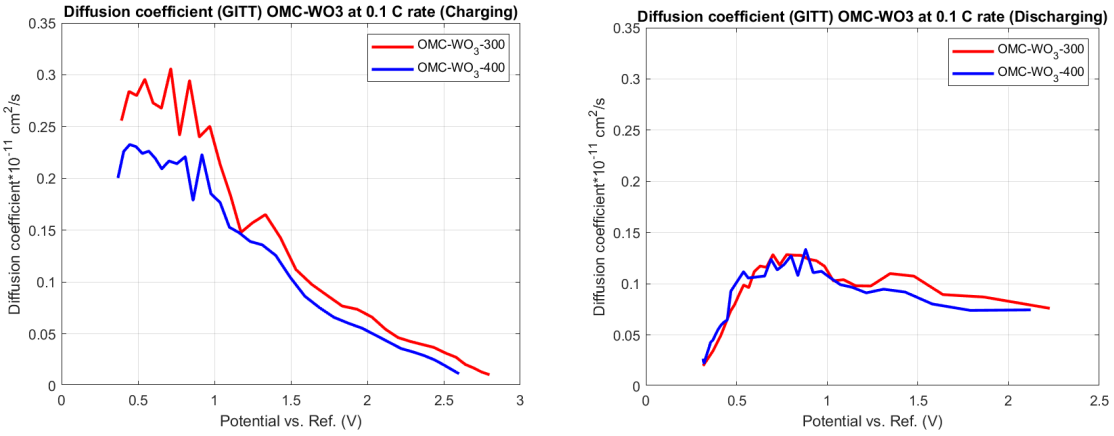

(a) **(b)**

Figure 3.20: Diffusion coefficient of the amorphous samples $OMC - WO_3 - 300$ and $OMC - WO_3 - 400$ (a) charging phase, (b) discharging phase

3.3.7 GCD rate performance and stability

The stability analysis of the investigated aprotic coin cells is performed based on the GCD technique at the rate at which the OMC coin cell is expected to provide the highest level of charge capacity equal to 4 mV/s in CV technique (figure 3.21, (a)). Additionally, the rate performance of WO_3-based cells is analyzed by applying the GCD method after performing the cells' initial stability and SEI layer creation. The higher specific capacity of the crystalline sample ($OMC - WO_3 - 600$) in comparison with the other amorphous hybrid samples is obvious in figure 3.21. Interestingly, despite the lower specific capacity of hybrid amorphous samples, which is around 80 mAg^{-1}, this value remains stable after 2600 cycles. Additionally, even though the $OMC - WO_3 - 600$ sample is not as stable as the amorphous ones, its high and almost stable specific capacity around 115 mAhg^{-1} after 1600 with comparatively high charging/discharging rate (560 mAg^{-1}) has made this sample the best choice. Concerning the OMC sample, its high stability after more than 2700 cycles is notable.

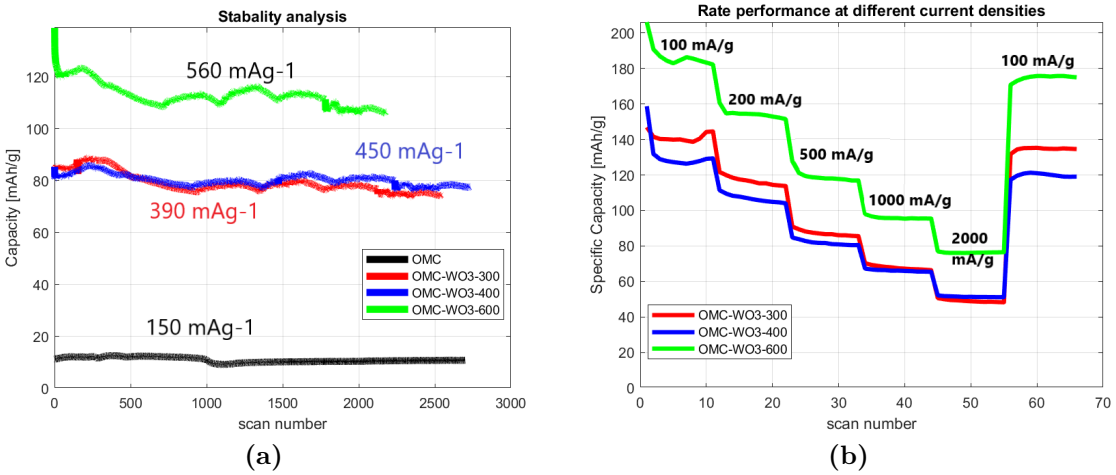

Figure 3.21: Aprotic coin cells (a) stability analysis, (b) Rate performance analysis based on GCD method

3.3.8 Literature review and summary

The table 3.6 provides a detailed comparison of the electrochemical properties of selected WO_3-based cells with Li-ion electrolyte in previous works.

Table 3.6: Comparison of electrochemical properties of selected WO_3-based cells with Li-ion based electrolyte

Material	**Specific capacity ($mAhg^{-1}$)**	**Current density (mAg^{-1})**	**Cycle number**	**Potential Window (V vs. RE)**	**ref**
WO_3 hollow microspheres	300	800	350	(0, 3)	[68]
Nb16W5O55 (NWO)	100	5c	1000	(0.5, 2.6)	[69]
amorphous WO_3	585	100	100	(0, 3)	[70]
WO_3-NR	300	80	50	(0.01, 2.5)	[71]
N-WOx	228	10000	4000	(0.01, 3)	[72]
WOx	117	10000	4000	(0.01, 3)	[72]
h-WO_3/NSG composites	196	1500	200	(0.05, 3)	[27]
Si–WO_3–C composite	400	50	50	(0.07, 1.5)	[73]
$OMC - WO_3 - 300$	75	390	2600	(0.25, 3.086)	this work
$OMC - WO_3 - 400$	80	459	2600	(0.25, 2.854)	this work
$OMC - WO_3 - 600$	115	569	1600	(0.2, 3.175)	this work

According to this comparison, the proposed fabricated cells would propose high stability (life cycle) in comparison with the previous works. The potential window close to 3 V can be more or less observed in the previous works. Moreover, in such high rate capabilities, the obtained capacity can be notable. However, comparing with [72], it seems that we still need to work on the WO_3 structure to reach higher rate capability and energy storage.

Chapter 4

Conclusion

4.1 Summary

In this project, we have demonstrated a hybrid material of WO_3 and ordered mesoporous carbon compounds. The low resistivity and high specific surface of the mesoporous carbon structure, and high ideal specific energy of WO_3, in addition to the high stability of both materials, have made this composition a suitable choice as the active electrode of an electrochemical cell with a high life cycle, rate capability, and capacity. OMC is produced by the hard template method; in subsequent, through the impregnation of PWA into the OMC, the hybrid material is prepared. After performing the thermal annealing at three different temperatures (300, 400, 600 C^o), amorphous hybrid samples are observed in the first two, while the WO_3 crystals appear after annealing the hybrid powder at 600 C^o ($OMC - WO_3 - 600$). Three electrochemical aqueous cells (H_2SO_4 water solution) based on OMC, $OMC - WO_3 - 300$, and $OMC - WO_3 - 400$ active materials are fabricated. The best results are obtained from the latter sample with 732 mAh^{-1} after 5000 cycles at the scan rate equal to 5 mVs^{-1}. Furthermore, considering the aprotic coin cell, the best electrochemical properties (stability, specific capacity, and rate capability) are observed at the $OMC - WO_3 - 600$ cell with a specific capacity equal to 114 mAh/g after 1600 cycles when the current density is 560 mA/g.

4.2 Future prospective

As future anticipation, providing a complete EES device is associated with investigating both anode and cathode of electrochemical energy storage and utilizing both electrodes for energy storing. Considering CV results of the water-based half cells, the OMC electrode is stable up to 1.02 V vs. reference, making it a suitable

material as a cathode in EES devices after defining $OMC - WO_3$ hybrid material as an anode. Consequently, we expect to obtain an EES device with around 1.3 V potential window. However, when it comes to the aprotic cells, the OMC samples have a more positive potential window (up to around 4 V vs. reference electrode) than hybrid samples. As a result, an EES device with around 3.8 V voltage range can be expected from the equivalent coin cell. The high stability of both anticipated anode ($OMC - WO_3$) and cathode (OMC) would make this device highly stable. Additionally, as mentioned before, the diffusion and surface-controlled charging mechanisms are most relevant at the hybrid and OMC electrodes, respectively. As a result, using these materials as the anode and cathode in an EES device would lead to a hybrid and asymmetric EES device, which is expected to provide both high energy storage and high charging/discharging rate.

Bibliography

[1] Maria R Lukatskaya, Bruce Dunn, and Yury Gogotsi. «Multidimensional materials and device architectures for future hybrid energy storage». In: *Nature communications* 7.1 (2016), pp. 1–13 (cit. on pp. 1, 6, 8, 11–14).

[2] Binson Babu, Patrice Simon, and Andrea Balducci. «Fast Charging Materials for High Power Applications». In: *Advanced Energy Materials* (2020), p. 2001128 (cit. on pp. 1–3, 5, 10, 19, 48).

[3] Xuehang Wang, Maryam Salari, De-en Jiang, Jennifer Chapman Varela, Babak Anasori, David J Wesolowski, Sheng Dai, Mark W Grinstaff, and Yury Gogotsi. «Electrode material–ionic liquid coupling for electrochemical energy storage». In: *Nature Reviews Materials* (2020), pp. 1–22 (cit. on pp. 1, 23).

[4] Patrice Simon, Yury Gogotsi, and Bruce Dunn. «Where do batteries end and supercapacitors begin?» In: *Science* 343.6176 (2014), pp. 1210–1211 (cit. on pp. 2, 4).

[5] M Rosa Palacin. «Recent advances in rechargeable battery materials: a chemist's perspective». In: *Chemical Society Reviews* 38.9 (2009), pp. 2565–2575 (cit. on p. 3).

[6] Pragati A Shinde and Seong Chan Jun. «Review on Recent Progress in the Development of Tungsten Oxide Based Electrodes for Electrochemical Energy Storage». In: *ChemSusChem* 13.1 (2020), pp. 11–38 (cit. on pp. 3, 4, 20–22).

[7] Patrice Simon and Yury Gogotsi. «Materials for electrochemical capacitors». In: *Nanoscience and technology: a collection of reviews from Nature journals*. World Scientific, 2010, pp. 320–329 (cit. on p. 4).

[8] Arie Borenstein, Ortal Hanna, Ran Attias, Shalom Luski, Thierry Brousse, and Doron Aurbach. «Carbon-based composite materials for supercapacitor electrodes: a review». In: *Journal of Materials Chemistry A* 5.25 (2017), pp. 12653–12672 (cit. on pp. 4, 6).

[9] Alessandro Pedico, Andrea Lamberti, Arnaud Gigot, Marco Fontana, Federico Bella, Paola Rivolo, Matteo Cocuzza, and Candido Fabrizio Pirri. «High-performing and stable wearable supercapacitor exploiting rGO aerogel decorated with copper and molybdenum sulfides on carbon fibers». In: *ACS Applied Energy Materials* 1.9 (2018), pp. 4440–4447 (cit. on p. 4).

[10] Thomas Christen and Martin W Carlen. «Theory of Ragone plots». In: *Journal of power sources* 91.2 (2000), pp. 210–216 (cit. on p. 4).

[11] Sanliang Zhang and Ning Pan. «Supercapacitors performance evaluation». In: *Advanced Energy Materials* 5.6 (2015), p. 1401401 (cit. on pp. 5, 16, 18).

[12] Jingsong Huang, Bobby G Sumpter, and Vincent Meunier. «Theoretical model for nanoporous carbon supercapacitors». In: *Angewandte Chemie* 120.3 (2008), pp. 530–534 (cit. on pp. 6, 7).

[13] Simon Fleischmann, James B Mitchell, Ruocun Wang, Cheng Zhan, De-en Jiang, Volker Presser, and Veronica Augustyn. «Pseudocapacitance: From Fundamental Understanding to High Power Energy Storage Materials». In: *Chemical Reviews* 120.14 (2020), pp. 6738–6782 (cit. on pp. 9, 10, 15, 18, 51, 61).

[14] Li Guan, Linpo Yu, and George Z Chen. «Capacitive and non-capacitive faradaic charge storage». In: *Electrochimica Acta* 206 (2016), pp. 464–478 (cit. on p. 11).

[15] Noémie Elgrishi, Kelley J Rountree, Brian D McCarthy, Eric S Rountree, Thomas T Eisenhart, and Jillian L Dempsey. «A practical beginner's guide to cyclic voltammetry». In: *Journal of chemical education* 95.2 (2018), pp. 197–206 (cit. on pp. 11, 37).

[16] Henri-Louis Girard, Bruce Dunn, and Laurent Pilon. «Simulations and interpretation of three-electrode cyclic voltammograms of pseudocapacitive electrodes». In: *Electrochimica Acta* 211 (2016), pp. 420–429 (cit. on p. 12).

[17] Hongta Yang and Peng Jiang. «Large-scale colloidal self-assembly by doctor blade coating». In: *Langmuir* 26.16 (2010), pp. 13173–13182 (cit. on p. 12).

[18] Liuchuan Tong, Yan Jing, Roy G Gordon, and Michael J Aziz. «Symmetric all-quinone aqueous battery». In: *ACS Applied Energy Materials* 2.6 (2019), pp. 4016–4021 (cit. on p. 13).

[19] Ping Wang et al. «Porous carbon for high-energy density symmetrical supercapacitor and lithium-ion hybrid electrochemical capacitors». In: *Chemical Engineering Journal* 375 (2019), p. 122020 (cit. on p. 13).

[20] Torsten Brezesinski, John Wang, Robert Senter, Kirstin Brezesinski, Bruce Dunn, and Sarah H Tolbert. «On the correlation between mechanical flexibility, nanoscale structure, and charge storage in periodic mesoporous CeO2 thin films». In: *ACS nano* 4.2 (2010), pp. 967–977 (cit. on pp. 15, 16).

[21] Tyler S Mathis, Narendra Kurra, Xuehang Wang, David Pinto, Patrice Simon, and Yury Gogotsi. «Energy storage data reporting in perspective—guidelines for interpreting the performance of electrochemical energy storage systems». In: *Advanced Energy Materials* 9.39 (2019), p. 1902007 (cit. on pp. 16, 36, 37, 49).

[22] Bryan Hirschorn, Mark E Orazem, Bernard Tribollet, Vincent Vivier, Isabelle Frateur, and Marco Musiani. «Determination of effective capacitance and film thickness from constant-phase-element parameters». In: *Electrochimica acta* 55.21 (2010), pp. 6218–6227 (cit. on p. 18).

[23] Chengdu Liang, Zuojiang Li, and Sheng Dai. «Mesoporous carbon materials: synthesis and modification». In: *Angewandte Chemie International Edition* 47.20 (2008), pp. 3696–3717 (cit. on p. 19).

[24] Bing Liu and Steve Creager. «Silica–sol-templated mesoporous carbon as catalyst support for polymer electrolyte membrane fuel cell applications». In: *Electrochimica acta* 55.8 (2010), pp. 2721–2726 (cit. on p. 19).

[25] Pragati A Shinde, Vaibhav C Lokhande, Nilesh R Chodankar, Taeksoo Ji, Jin Hyeok Kim, and Chandrakant D Lokhande. «Enhanced electrochemical performance of monoclinic WO3 thin film with redox additive aqueous electrolyte». In: *Journal of colloid and interface science* 483 (2016), pp. 261–267 (cit. on pp. 20, 53).

[26] Xiaochuan Duan, Songhua Xiao, Lingling Wang, Hui Huang, Yuan Liu, Qiuhong Li, and Taihong Wang. «Ionic liquid-modulated preparation of hexagonal tungsten trioxide mesocrystals for lithium-ion batteries». In: *Nanoscale* 7.6 (2015), pp. 2230–2234 (cit. on p. 20).

[27] Yiqiao Huang, Ruiming Lu, Michael Wang, Jeff Sakamoto, and Pierre FP Poudeu. «Hexagonal-WO3 nanorods encapsulated in nitrogen and sulfur co-doped reduced graphene oxide as a high-performance anode material for lithium ion batteries». In: *Journal of Solid State Chemistry* 282 (2020), p. 121068 (cit. on pp. 20, 21, 55–57, 66).

[28] Tao Zhu, Meng Nan Chong, and Eng Seng Chan. «Nanostructured tungsten trioxide thin films synthesized for photoelectrocatalytic water oxidation: a review». In: *ChemSusChem* 7.11 (2014), pp. 2974–2997 (cit. on p. 22).

[29] Ruiyong Chen, Dominic Bresser, Mohit Saraf, Patrick Gerlach, Andrea Balducci, Simon Kunz, Daniel Schröder, Stefano Passerini, and Jun Chen. «A comparative review of electrolytes for organic material-based energy storage devices employing solid electrodes and redox fluids». In: *ChemSusChem* (2020) (cit. on pp. 23, 25).

[30] *Pourbaix diagram.* URL: https://en.wikipedia.org/wiki/Pourbaix_diagram# (cit. on p. 24).

[31] J Bard Allen and R Faulkner Larry. *Electrochemical methods fundamentals and applications.* John Wiley & Sons, 2001 (cit. on pp. 27, 28).

[32] Autolab Application Note EC08. «Basic overview of the working principle of a potentiostat/galvanostat (PGSTAT)–Electrochemical cell setup». In: *Metrohm Autolab. BV* (2011), pp. 1–3 (cit. on p. 28).

[33] LD Whittig and WR Allardice. «X-ray diffraction techniques». In: *Methods of Soil Analysis: Part 1 Physical and Mineralogical Methods* 5 (1986), pp. 331–362 (cit. on p. 31).

[34] WILLIE Harris and G Norman White. «X-ray diffraction techniques for soil mineral identification». In: *Methods of soil analysis part 5—Mineralogical methods* 5 (2008), pp. 81–115 (cit. on p. 31).

[35] *MyScope: Microscopy training (SEM).* URL: https://myscope.training/#/SEMlevel_3_1 (cit. on p. 31).

[36] Vasile-Dan Hodoroaba. «Chapter 4.4 - Energy-dispersive X-ray spectroscopy (EDS)». In: *Characterization of Nanoparticles.* Ed. by Vasile-Dan Hodoroaba, Wolfgang E S Unger, and Alexander G Shard. Micro and Nano Technologies. Elsevier, 2020, pp. 397–417. ISBN: 978-0-12-814182-3. DOI: https://doi.org/10.1016/B978-0-12-814182-3.00021-3. URL: https://www.sciencedirect.com/science/article/pii/B9780128141823000213 (cit. on p. 32).

[37] Katchala Nanaji, Tata N Rao, UV Varadaraju, and Srinivasan Anandan. «Pore Size-Engineered Three-Dimensional Ordered Mesoporous Carbons with Improved Electrochemical Performance for Supercapacitor and Lithium-ion Battery Applications». In: *ChemistrySelect* 4.34 (2019), pp. 10104–10112 (cit. on p. 32).

[38] Stalin Joseph, Devaraju M Kempaiah, Mercy R Benzigar, Hamid Ilbeygi, Gurwinder Singh, Siddulu Naidu Talapaneni, Dae-Hwan Park, and Ajayan Vinu. «Highly ordered mesoporous carbons with high specific surface area from carbonated soft drink for supercapacitor application». In: *Microporous and Mesoporous Materials* 280 (2019), pp. 337–346 (cit. on p. 32).

[39] Juqin Zeng, Carlotta Francia, Mihaela A Dumitrescu, Alessandro HA Monteverde Videla, Vijaykumar S Ijeri, Stefania Specchia, and Paolo Spinelli. «Electrochemical performance of Pt-based catalysts supported on different ordered mesoporous carbons (Pt/OMCs) for oxygen reduction reaction». In: *Industrial & engineering chemistry research* 51.22 (2012), pp. 7500–7509 (cit. on p. 33).

[40] J Zeng, C Francia, C Gerbaldi, V Baglio, S Specchia, AS Aricò, and P Spinelli. «Hybrid ordered mesoporous carbons doped with tungsten trioxide as supports for Pt electrocatalysts for methanol oxidation reaction». In: *Electrochimica Acta* 94 (2013), pp. 80–91 (cit. on pp. 33, 34, 49).

[41] Yusuke Izumi and Kazuo Urabe. «Catalysis of heteropoly acids entrapped in activated carbon». In: *Chemistry Letters* 10.5 (1981), pp. 663–666 (cit. on p. 34).

[42] MA Schwegler, P Vinke, M Van der Eijk, and H Van Bekkum. «Activated carbon as a support for heteropolyanion catalysts». In: *Applied Catalysis A: General* 80.1 (1992), pp. 41–57 (cit. on p. 34).

[43] Pawel J Kulesza, Malgorzata Chojak, Katarzyna Karnicka, Krzysztof Miecznikowski, Barbara Palys, Adam Lewera, and Andrzej Wieckowski. «Network films composed of conducting polymer-linked and polyoxometalate-stabilized platinum nanoparticles». In: *Chemistry of materials* 16.21 (2004), pp. 4128–4134 (cit. on p. 34).

[44] Verónica Palomares, Aintzane Goñi, Izaskun Gil De Muro, Iratxe De Meatza, Miguel Bengoechea, Igor Cantero, and Teófilo Rojo. «Conductive additive content balance in Li-ion battery cathodes: Commercial carbon blacks vs. in situ carbon from LiFePO4/C composites». In: *Journal of Power Sources* 195.22 (2010), pp. 7661–7668 (cit. on p. 34).

[45] Murilo Santhiago, Cátia C Corrêa, Juliana S Bernardes, Mariane P Pereira, Let'ıcia JM Oliveira, Mathias Strauss, and Carlos CB Bufon. «Flexible and foldable fully-printed carbon black conductive nanostructures on paper for high-performance electronic, electrochemical, and wearable devices». In: *ACS applied materials & interfaces* 9.28 (2017), pp. 24365–24372 (cit. on p. 34).

[46] Boris Dyatkin, Volker Presser, Min Heon, Maria R Lukatskaya, Majid Beidaghi, and Yury Gogotsi. «Development of a green supercapacitor composed entirely of environmentally friendly materials». In: *ChemSusChem* 6.12 (2013), pp. 2269–2280 (cit. on p. 34).

[47] Qamar Abbas, Dorota Pajak, Elżbieta Frąckowiak, and François Béguin. «Effect of binder on the performance of carbon/carbon symmetric capacitors in salt aqueous electrolyte». In: *Electrochimica Acta* 140 (2014), pp. 132–138 (cit. on p. 34).

[48] Bin Xu, Haoran Wang, Qizhen Zhu, Ning Sun, Babak Anasori, Longfeng Hu, Feng Wang, Yibiao Guan, and Yury Gogotsi. «Reduced graphene oxide as a multi-functional conductive binder for supercapacitor electrodes». In: *Energy Storage Materials* 12 (2018), pp. 128–136 (cit. on p. 34).

[49] CR Birkl, Euan McTurk, MR Roberts, PG Bruce, and DA Howey. «A parametric open circuit voltage model for lithium ion batteries». In: *Journal of The Electrochemical Society* 162.12 (2015), A2271 (cit. on p. 35).

[50] Mark A Bissett, Ian A Kinloch, and Robert AW Dryfe. «Characterization of MoS2–graphene composites for high-performance coin cell supercapacitors». In: *ACS applied materials & interfaces* 7.31 (2015), pp. 17388–17398 (cit. on p. 35).

[51] Yufeng Han, Jixiao Wang, Hairui Zhang, Song Zhao, Qiang Ma, and Zhi Wang. «Electrochemical impedance spectroscopy (EIS): an efficiency method to monitor resin curing processes». In: *Sensors and Actuators A: Physical* 250 (2016), pp. 78–86 (cit. on p. 35).

[52] C John Wen, BA Boukamp, Robert A Huggins, and W Weppner. «Thermodynamic and mass transport properties of "LiAl"». In: *Journal of The Electrochemical Society* 126.12 (1979), p. 2258 (cit. on p. 39).

[53] *Autolab Application Note BAT03, Galvanostatic Intermittent Titration Technique*. URL: `https://www.ecochemie.nl/download/Applicationnotes/Autolab_Application_Note_BAT03.pdf` (cit. on p. 39).

[54] Edoardo Besozzi, David Dellasega, Valeria Russo, C Conti, M Passoni, and MG Beghi. «Thermomechanical properties of amorphous metallic tungsten-oxygen and tungsten-oxide coatings». In: *Materials & Design* 165 (2019), p. 107565 (cit. on pp. 40, 41, 64).

[55] B Pecquenard, H Lecacheux, J Livage, and C Julien. «Orthorhombic wo3formed via a ti-stabilized wo3 · 13h2o phase». In: *Journal of Solid State Chemistry* 135.1 (1998), pp. 159–168 (cit. on pp. 40, 41).

[56] Shaohong Wei, Junhong Zhao, Boxiao Hu, Kaiqiang Wu, Weimin Du, and Meihua Zhou. «Hydrothermal synthesis and gas sensing properties of hexagonal and orthorhombic WO3 nanostructures». In: *Ceramics International* 43.2 (2017), pp. 2579–2585 (cit. on p. 40).

[57] Meijia Qiu, Peng Sun, Liuxue Shen, Kun Wang, Shuqin Song, Xiang Yu, Shaozao Tan, Chuanxi Zhao, and Wenjie Mai. «WO 3 nanoflowers with excellent pseudo-capacitive performance and the capacitance contribution analysis». In: *Journal of Materials Chemistry A* 4.19 (2016), pp. 7266–7273 (cit. on p. 46).

[58] Hui Peng, Guofu Ma, Kanjun Sun, Jingjing Mu, Mengting Luo, and Ziqiang Lei. «High-performance aqueous asymmetric supercapacitor based on carbon nanofibers network and tungsten trioxide nanorod bundles electrodes». In: *Electrochimica Acta* 147 (2014), pp. 54–61 (cit. on pp. 47, 49).

[59] Wanmei Sun, Michael T Yeung, Andrew T Lech, Cheng-Wei Lin, Chain Lee, Tianqi Li, Xiangfeng Duan, Jun Zhou, and Richard B Kaner. «High surface area tunnels in hexagonal WO3». In: *Nano letters* 15.7 (2015), pp. 4834–4838 (cit. on p. 53).

[60] Debasish Mandal, Parimal Routh, and Arun K Nandi. «A new facile synthesis of tungsten oxide from tungsten disulfide: structure dependent supercapacitor and negative differential resistance properties». In: *Small* 14.4 (2018), p. 1702881 (cit. on p. 53).

[61] Changshin Jo, Ilkyu Hwang, Jinwoo Lee, Chul Wee Lee, and Songhun Yoon. «Investigation of pseudocapacitive charge-storage behavior in highly conductive ordered mesoporous tungsten oxide electrodes». In: *The Journal of Physical Chemistry C* 115.23 (2011), pp. 11880–11886 (cit. on p. 53).

[62] Shobhnath P Gupta, Harishchandra H Nishad, Sanjay D Chakane, Suresh W Gosavi, Dattatray J Late, and Pravin S Walke. «Phase transformation in tungsten oxide nanoplates as a function of post-annealing temperature and its electrochemical influence on energy storage». In: *Nanoscale Advances* 2.10 (2020), pp. 4689–4701 (cit. on p. 53).

[63] Ting Wang, Hui Liu, Junqi Li, and Hafiz Akif Munir. «Facile Preparation of h-WO3/Carbon Cloth Nanocomposite and Its Electrochemical Properties for Supercapacitors». In: *ChemistrySelect* 5.26 (2020), pp. 7704–7713 (cit. on p. 53).

[64] Zhiwei Liu, Ping Li, Yuan Dong, Qi Wan, Fuqiang Zhai, Alex A Volinsky, and Xuanhui Qu. «Facile preparation of hexagonal WO3 · 0.33 H2O/C nanostructures and its electrochemical properties for lithium-ion batteries». In: *Applied surface science* 394 (2017), pp. 70–77 (cit. on pp. 55, 57).

[65] Pu Li, Xing Li, Ziyan Zhao, Mingshan Wang, Thomas Fox, Qian Zhang, and Ying Zhou. «Correlations among structure, composition and electrochemical performances of WO3 anode materials for lithium ion batteries». In: *Electrochimica Acta* 192 (2016), pp. 148–157 (cit. on pp. 56, 57).

[66] Ying Sun, Wei Wang, Jinwen Qin, Di Zhao, Baoguang Mao, Ying Xiao, and Minhua Cao. «Oxygen vacancy-rich mesoporous W18O49 nanobelts with ultrahigh initial Coulombic efficiency toward high-performance lithium storage». In: *Electrochimica Acta* 187 (2016), pp. 329–339 (cit. on p. 57).

[67] Henrik Lindström, Sven Södergren, Anita Solbrand, Håkan Rensmo, Johan Hjelm, Anders Hagfeldt, and Sten-Eric Lindquist. «Li+ ion insertion in TiO2 (anatase). 2. Voltammetry on nanoporous films». In: *The Journal of Physical Chemistry B* 101.39 (1997), pp. 7717–7722 (cit. on p. 61).

[68] Hui Tong, Yingming Xu, Xiaoli Cheng, Xianfa Zhang, Shan Gao, Hui Zhao, and Lihua Huo. «One-pot solvothermal synthesis of hierarchical WO3 hollow microspheres with superior lithium ion battery anode performance». In: *Electrochimica Acta* 210 (2016), pp. 147–154 (cit. on p. 66).

[69] Yumi Kim, Quentin Jacquet, Kent J Griffith, Jeongjae Lee, Sunita Dey, Bernardine LD Rinkel, and Clare P Grey. «High Rate Lithium Ion Battery with Niobium Tungsten Oxide Anode». In: *Journal of The Electrochemical Society* 168.1 (2021), p. 010525 (cit. on p. 66).

[70] Bao Yang, Peixian Miao, and Jingzhong Cui. «Characteristics of amorphous WO 3 thin films as anode materials for lithium-ion batteries». In: *Journal of Materials Science: Materials in Electronics* 31 (2020), pp. 11071–11076 (cit. on p. 66).

[71] Raman Bekarevich et al. «Conversion Reaction in the Binder-Free Anode for Fast-Charging Li-Ion Batteries Based on WO3 Nanorods». In: *ACS Applied Energy Materials* 3.7 (2020), pp. 6700–6708 (cit. on p. 66).

[72] Yanglansen Cui, Kefeng Xiao, Nicholas M Bedford, Xinxin Lu, Jimmy Yun, Rose Amal, and Da-Wei Wang. «Refilling nitrogen to oxygen vacancies in ultrafine tungsten oxide clusters for superior lithium storage». In: *Advanced Energy Materials* 9.37 (2019), p. 1902148 (cit. on p. 66).

[73] Hyun-seung Kim, Jongjung Kim, Jae Gil Lee, Ji Heon Ryu, Jaekwang Kim, Seung M Oh, and Songhun Yoon. «Novel silicon–tungsten oxide–carbon composite as advanced negative electrode for lithium-ion batteries». In: *Solid State Ionics* 314 (2018), pp. 41–45 (cit. on p. 66).